Targeting N-acetyl-L-aspartate synthesis and transport for treatment of Canavan leukodystrophy

By

VANESSA L. HULL
DISSERTATION

Submitted in partial satisfaction of the requirements for the degree of

DOCTOR OF PHILOSOPHY

in

Neuroscience

in the

OFFICE OF GRADUATE STUDIES

of the

UNIVERSITY OF CALIFORNIA

DAVIS

Approved:

David Pleasure, Chair

Laura N. Borodinsky

Fuzheng Guo

Anna La Torre

Aijun Wang

Committee in Charge

2023

ACKNOWLEDGEMENTS

The unwavering support of my mentor, Dr. David Pleasure, has been instrumental in my professional development and my growth as a scientist. I am eternally grateful for your patience, wisdom and sense of humor, all of which have led me through the most challenging of moments with tremendous grace. I must also express my gratitude for the mentorship and guidance of Dr. Laura N. Borodinsky, who has truly set the standard for the type of mentor I aspire to be one day. Dr. Fuzheng Guo, you and your team have been a constant source of experimental guidance and encouragement. Dr. Valentina Medici, thank you for believing in me from day one. There are a whole host of other mentors I'd like to acknowledge, including Dr. Athena Soulika, Dr. Anna La Torre, Dr. Paul Knoepfler, and Dr. Aijun Wang.

I have been fortunate enough to have built a strong international network of colleagues and friends that have all have been rendered in cartoon form at least once by now. Dr. Yan Wang: you have saved me so many times, I am proud to call you Meimei. Travis Burns: you kept me sane and contributed constant effort to countless projects over the years. My cohort-mates and friends Joey Charbonneau, who recently finally advanced to candidacy, and Dr. Greg Disse: physical proximity has never defined our friendship and I hope this trend continues. Dr. Carmen Falcone: even though you are in Europe now, you are still the person I run to immediately with every success and every setback. We have been through many stages in life together and I appreciate our friendship beyond measure. Dr. Alex Panoutsopoulos and Dr. Olga Balashova: we survived the pandemic together thanks to years of inoculation with Shriner's toxic coffee. Cheers to our continued perseverance.

I would like to recognize the support I have had from my family. Thank you to my father David, who put a wrench in my hand when I was a little girl and taught me how to lean into life's many twists and turns. Thank you to my sister Tiffany who has been a first rate Auntie and gave me the most precious gift: my niece Ellie. For my grandparents Joan and Cordell, whom I miss

dearly and wish were here to share in this moment. Thank you to my mother Rebecca who, in spite of our differences, I recognize as having a good heart and only the best intentions. I must also acknowledge the overwhelming support I draw from my expanded family as I am so fortunate to now stand alongside strong women like you, Jan, Mary and Diane.

I'll close my acknowledgements by recognizing those poor souls that have had the extreme misfortunate of having to share a roof with me and therefore, suffer daily. First, a man who deserves his own dissertation for tolerating my nonsense over the years, my partner Michael Casha. You remain constant in your calm and grounding energy even as the eye of the storm (me) circles around you. I am most grateful for the core of our life together: our creative and bright son Jackson. Jackson, you have truly started to become your own little person as of late. Your boundless curiosity about the world inspires me and challenges me daily. Dad and I are so proud of you. Finally, I would be remiss if I didn't recognize the tireless efforts of Emma the dog, who patiently awaits my arrival home from lab every single day, even if it's 12 AM. You are always excited to see me, even on the days when I'm not excited to see myself. You never care how unkempt I am or how many experiments I've ruined, and to me this represents love in its purest form.

ABSTRACT

Canavan disease (CD) is an incurable, progressive leukodystrophy that develops in infancy as the result of *Aspa* mutations which disrupt the functionality of aspartoacylase (ASPA). ASPA is an oligodendroglial-enriched enzyme responsible for cleaving the abundant brain amino acid, N-acetyl-L-aspartate (NAA). As a result, infants and children with CD are unable to metabolize NAA and have extremely elevated levels of brain NAA accompanied by spongiform white matter degeneration, motor and cognitive delays, ataxia, and progressive neuronal atrophy. Attempts at ASPA gene replacement have proven largely ineffective, resulting in an urgent need to define new therapeutic targets for this fatal disease.

We hypothesize that the primary mechanism of Canavan disease pathophysiology is brain toxicity resulting from elevated NAA. Indeed, constitutive knockout of the NAA-synthesizing enzyme NAT8L (N-acetyltransferase-8-like) is protective against development of vacuolar leukodystrophy and ataxia in the well characterized CD model mouse (*Aspa*$^{nur7/nur7}$, "CD mouse"). The current body of work is based upon this "NAA toxicity" hypothesis, with an emphasis on developing and testing translational therapies for CD.

In the first study, I treated adult, symptomatic CD mice with an antisense oligonucleotide (ASO) targeting the knockdown of NAT8L. Intracisternal delivery of this NAT8L ASO lowers NAA levels and improves motor function and brain vacuolation within 2 weeks. In the second study, we identified a sodium-coupled dicarboxylate plasma membrane transporter (NaDC3) with a high affinity for NAA that is exclusively expressed by astrocytes in the parenchyma. Operating under the hypothesis that vacuolar degeneration and fluid retention in CD is the result of sodium/NAA overloading specifically in astrocytes, I generated CD mice with constitutive ablation of NaDC3. Indeed, NaDC3 knockout prevents the development of leukodystrophy and ataxia in CD mice. Ongoing studies seek to determine the benefit of astroglial-specific conditional NaDC3 knockout, given that NaDC3 is also highly expressed in the meninges and kidney.

The strong astroglial phenotypes observed in CD, coupled with Purkinje cell dendritic abnormalities that I was the first to report in CD mice, led me to the radial astrocytes of the cerebellum, the Bergmann glia. I hypothesize that Bergmann glia exert a non-cell autonomous mechanism for Purkinje cell dysfunction in CD. In the third and final study, I report profound Bergmann glia structural damage in CD mice in concert with prolonged, less frequent calcium signals in Bergmann glial processes. Importantly, NAT8L ASO therapy improves the structural integrity of both Bergmann glia and Purkinje cells.

Overall, I demonstrate that lowering NAA, either by blocking its synthesis or cellular uptake, is therapeutic for CD mice. I also present a novel, astroglial-centric perspective on CD pathogenesis. We are encouraged by the translatability of these findings, and as such, I conclude with a summary of remaining questions in the field of CD research as well as future directions for CD therapy.

Table of Contents

ACKNOWLEDGEMENTS **2**

ABSTRACT **4**

CHAPTER 1— INTRODUCTION **1**

1.1 CANAVAN DISEASE: EARLY CLINICAL FEATURES AND ETIOLOGY 1
1.2 THE OLIGODENDROGLIAL STARVATION HYPOTHESIS 2
1.3 NAA TOXICITY HYPOTHESIS 3
1.4 ASTROGLIAL UPTAKE OF NAA BY THE MEMBRANE TRANSPORTER NADC3* 4
1.5 BERGMANN GLIA PATHOLOGY IN CANAVAN DISEASE 5
1.7 DISSERTATION OVERVIEW 5

CHAPTER 2 — ANTISENSE OLIGONUCLEOTIDE REVERSES LEUKODYSTROPHY AND IN CANAVAN DISEASE MICE **7**

2.1 ABSTRACT 7
2.2 INTRODUCTION 7
2.3 MATERIALS AND METHODS 8
2.4 RESULTS 9
2.5 DISCUSSION 14

CHAPTER 3 — ABLATING THE SODIUM DICARBOXYLIC ACID TRANSPORTER NADC3 PREVENTS LEUKODYSTROPHY IN CANAVAN DISEASE MICE **16**

3.1 ABSTRACT 16
3.2 INTRODUCTION 16
3.3 MATERIALS AND METHODS 17
3.4 RESULTS 19
3.5 DISCUSSION 23

CHAPTER 4 — PATHOLOGICAL BERGMANN GLIA ALTERATIONS AND DISRUPTED CALCIUM DYNAMICS IN ATAXIC CANAVAN DISEASE MICE **25**

4.1 ABSTRACT 25
4.2 INTRODUCTION 26
4.3 METHODS 27
4.4 RESULTS 30
4.5 DISCUSSION 42

CHAPTER 5 — CONCLUSIONS **48**

5.1 SUMMARY 48
5.2 NAA AS A MARKER OF NEURONAL HEALTH 48
5.3 NAA NEUROTOXICITY 49
5.4 NAA-G 50
5.5 *SLC13A3*/NADC3 IN CANAVAN DISEASE 51
5.6 ASTROGLIA IN CANAVAN DISEASE 52
5.7 THE FUTURE OF CANAVAN DISEASE THERAPY 53

REFERENCES **55**

List of Figures

Figure 2.1: Effects of intracisternal Nat8l gapmer on cerebellar Nat8l mRNA abundance, [NAA_B], and accelerating rotarod performance……..……..……..…...10

Figure 2.2: Effects of intracisternal Nat8l gapmer on cerebellar white matter vacuolation and oligodendroglial numbers and on thalamic vacuolation and GFAP immunoreactivity in CD mice...11

Figure 2.3: Effects of intracisternal Nat8l gapmer on Purkinje cell dendrite length and dendritic spine density in CD mice……..……..……..13

Figure 3.1: Comparison of the renal and brain *Slc13a3* mRNA and NaDC3 expression between *Slc13a3*$^{WT/WT}$ and *Slc13a3*$^{KO/KO}$ mice……...……..20

Figure 3.2: Constitutive *Slc13a3*$^{KO/KO}$ does not alter expression levels of myelin proteins in *Aspa*$^{WT/WT}$ cerebellum between p7 and p60, nor alter p7-p60 abundances of neuronal (*Nat8l*), astroglial (*Gfap*), or oligodendroglial lineage (*Pdgfra*, *Tcf7l2*, *Mag*, *Mbp*) marker mRNAs in *Aspa*$^{WT/WT}$ spinal cord……..21

Figure 3.3: Constitutive *Slc13a3*$^{KO/KO}$ increases urinary NAA output, normalizes [NAA_B], enhances weight gain and rotarod performance, and prevents brain vacuolation in CD mice…..……..…...22

Figure 4.1: Canavan disease mice present with ataxia and widespread brain vacuolation……..…...31

Figure 4.2: Bergman glia exhibit discontinuous, swollen processes and irregular somatic morphology and position in Canavan disease mice……..……..…….32

Figure 4.3: Bergmann glia-Purkinje cell interactions are disrupted in Canavan disease mice…..…...33

Figure 4.4: Loss of parallel fiber-/climbing fiber-Purkinje cell synapses in Canavan disease mice…35

Figure 4.5: Bergmann glia exhibit a loss of Ca^{2+}-permeable AMPARs and glutamate transporters in Canavan disease mice……..……...36

Figure 4.6: Bergmann glia and Purkinje cell alterations appear between p14 and p21 in Canavan disease mice ……..…….…..37

Figure 4.7: Bergmann glia Ca^{2+} transients are less frequent/prolonged in Canavan disease mice..38

Figure 4.8: Antisense oligonucleotide therapy repairs Bergmann glia irregularities observed in Canavan disease mice……..……..…...41

Table 4.1: Antibodies and Primers……..……..47

CHAPTER 1– INTRODUCTION

1.1 CANAVAN DISEASE: EARLY CLINICAL FEATURES AND ETIOLOGY

Canavan disease, a rare, genetic pediatric leukodystrophy, was first described in 1931 by one of the earliest female neuropathologists, Dr. Myrtelle Canavan, when an infant presented with macrocephaly, nystagmus and failure to meet developmental milestones[1]. Subsequent histological studies revealed widespread spongiform brain degeneration and edema. Canavan disease became recognized as a clinically distinct entity in 1949 when van Bogaert and Bertrand identified similar spongiform neurodegeneration and hypotonia in a group of children of Ashkenazi Jewish descent.[2] Other primary features manifesting in infancy and childhood include poor head control, hypotonia, cognitive delays, feeding and swallowing difficulties, ataxia, and poor visual tracking.[3] As the disease progresses, children face progressive limb stiffness and spasticity, blindness, seizures and most will require placement of a feeding tube[4]. Cytotoxic lesions are evident by MRI in the forebrain, cerebellum and brainstem[5] and post mortem histological studies show prominent astroglial and intramyelinic vacuolation of the brain.[6–8] CD is typically fatal by the age of 10, though there are occasional later onset cases with a longer course[9].

In 1988 Matalon et al identified the biochemical origin of Canavan disease: defects in the enzyme aspartoacylase (ASPA), and subsequent cloning experiments in the late 1990s revealed the specific *Aspa* missense mutations that cause the disease[10]. ASPA is an oligodendroglial enzyme responsible for cleaving the metabolite, N-acetyl-L-aspartate (NAA), second only to glutamate in its brain abundance.[11] As a result of ASPA deficiency, infants and children with Canavan disease have substantially increased brain NAA concentrations, often double the normal amount.[12] Canavan disease patients also excrete excess NAA in their urine, making elevated urinary NAA a primary indicator for disease diagnosis.[9]

Biallelic loss of function *Aspa* mutations are responsible for infantile onset Canavan disease, the most common and most severe form. While the incidence in the general population is rare (approximately 1:100,000 births), it is highly prevalent among individuals of Ashkenazi Jewish heritage, where the carrier frequency is 1:40.[11,13] 97% of Ashkenazi Jewish Canavan disease patients have either (1) a missense mutation at codon 285 (Glu →Ala; 84% of cases) or (2) a nonsense mutation at codon 231 (tyrosine → stop codon; 13% of cases).[14] While a higher diversity of *Aspa* mutations is found in non-Jewish Canavan disease cases, owing to novel polymorphisms, a slight majority of individuals have a missense mutation at codon 305 (Ala → Glu: 33% of cases).[13,14] Heterozygous individuals with one fully functional copy of *Aspa*, and therefore ~50% of the normal amount of functional ASPA protein, can breakdown NAA sufficiently such that their cognitive and motor development proceed normally.[15] Later onset forms of Canavan disease with decreased symptom severity are often the result of biallelic mutations that result in 25% or less of normal ASPA activity[16].

Attempts at *Aspa* gene replacement therapy and other treatment protocols involving dietary interventions and anti-convulsant medications have proven ineffective at improving motor deficits and brain vacuolation and are unable to stop disease progression.[17,18] For these reasons, there is a critical need to identify novel therapeutic targets for Canavan disease. Why and how aspartoacylase deficiency leads to vacuolar leukodystrophy has been a matter of some debate, with two leading theories: the “oligodendroglial starvation” hypothesis and the “NAA toxicity” hypothesis.

1.2 THE OLIGODENDROGLIAL STARVATION HYPOTHESIS

ASPA catalyzes deacetylation of NAA which allows oligodendrocytes to generate free acetate, an important precursor for acetyl-CoA and subsequent myelin synthesis.[19] The “oligodendroglial starvation” hypothesis contends that this loss of crucial acetate leads to the

prominent dysmyelinated phenotype observed in Canavan disease. Evidence in support of this hypothesis comes from studies showing that brain acetyl-CoA concentrations are decreased in aspartoacylase-null mice.[12] Additionally, an *in vivo* study involving intracerebral injection of radiolabeled NAA, shows that acetyl groups derived from NAA are rapidly incorporated into myelin lipids during myelination in developing rats.[20]

The "oligodendroglial starvation" hypothesis has been weakened, however, by work from our lab wherein we generated mice with constitutive deletion of the NAA synthesizing enzyme N-acetyltransferase-8-like (Nat8l) and saw no evidence of disrupted myelination in mice.[21] Aspartoacylase deficient mice (*Aspa*$^{nur7/nur7}$, "CD mice") are a well characterized model for Canavan disease that exhibit elevated NAA, ataxia and intramyelinic/astroglial vacuolation.[22] Similarly, normal myelination is seen in CD mice when we constitutively ablate Nat8l and, by extension, NAA.[21] Importantly, Nat8l knockout also protects against ataxia and brain vacuolation in CD mice.[21] In the single case reported to date of a patient with hypoacetylaspartia, the complete absence of NAA and its derivative NAA-glutamic acid (NAA-G; discussed further in Chapter 5: Conclusions) was associated with mild developmental and speech delay but no major changes in myelination, brain morphology or motor function.[23]

1.3 NAA TOXICITY HYPOTHESIS

An alternative "NAA toxicity" hypothesis contends that elevation of NAA in Canavan disease and CD mice causes brain osmotic dysregulation, resulting in astroglial and intramyelinic vacuolation. This hypothesis has been strengthened by our aforementioned study where constitutive Nat8l knockout in CD mice prevents vacuolar leukodystrophy, but also by a second study from our lab showing that intracerebroventricular administration of an adeno-associated viral vector (AAV) containing a short hairpin RNA that inhibits *Nat8l* translation to neonatal CD mice almost completely protects them against vacuolar leukodystrophy.[24] Chapter 2 describes

how disease progression can also be reversed in adult CD mice by blocking the synthesis of NAA with an antisense oligonucleotide.[25] This combined body of evidence supports the idea that brain vacuolation and motor deficits observed in Canavan disease are a direct consequence of elevated NAA in the brain and that, importantly, *they can be reversed by lowering brain NAA.*

1.4 ASTROGLIAL UPTAKE OF NAA BY THE MEMBRANE TRANSPORTER NADC3

Despite being metabolized by ASPA hydrolysis in oligodendrocytes, NAA is actually synthesized in the mitochondria of neurons by the enzyme NAT8L (N-acetyltransferase 8 like).[11] NAT8L acetylates L-aspartate by borrowing an acetyl group from acetyl-CoA, thereby converting the amino acid into the hydrophilic carboxylate N-acetyl-L-aspartate (NAA). The next step in the multicellular metabolic transport pathway of NAA has yet to be fully elucidated, given that oligodendrocytes do not possess any known uptake mechanism for NAA.

Astrocytes do, however, express the sodium-coupled dicarboxylic acid transporter NaDC3 (encoded by *Slc13a3*) which has a moderately high affinity for NAA.[26,27] NaDC3 is well suited for NAA uptake given that the K_m = 95 µM in rodent astrocyte cultures[28] and the NAA concentration in the interstitial space is around 80-100 µM in rats.[29] Cultured rat primary astrocytes, in addition to transfected HEK cells expressing NaDC3, have been shown to rapidly uptake NAA.[26,30] The sodium-coupled uptake of NAA (3 Na^+ ions per NAA molecule)[26] could result in astroglial swelling and water dysregulation, given ASPA deficiency in oligodendrocytes, which are connected to astrocytes via heterodimeric gap junctions[31]. Indeed, deletion of the connexin proteins (CX47 and CX43) that make up these astroglial-oligodendroglial gap junctions results in brain vacuolation and diminished rotarod retention times, underscoring the importance of solute transport between these two cell types for healthy brain osmoregulation.[32,33] Based on the hypothesis that astroglial overloading with NAA and Na^+ is a major driver of Canavan disease vacuolation and ataxia,

Chapter 3 will show that constitutive ablation of the transporter NaDC3 can prevent brain vacuolation and ataxia in CD mice.

1.5 BERGMANN GLIA PATHOLOGY IN CANAVAN DISEASE

Considering the astroglial disturbances and the Purkinje cell dendritic abnormalities observed in CD mice, I became curious about the Purkinje cell-adjacent Bergmann glia. Bergmann glia are radial astrocytes responsible for directing the structural and functional development of the cerebellum, with critical roles in granule cell migration, Purkinje cell dendritogenesis and synaptogenesis of the molecular layer.[34,35] Chapter 4 explores the role of Bergmann glia in driving non-cell autonomous PC dysfunction in CD wherein I describe profound damage to Bergmann glia and Purkinje cells in CD mice, many features of which are rescued by *Nat8l* ASO administration.

1.7 DISSERTATION OVERVIEW

The overarching hypothesis underlying this body of work is that Canavan disease pathophysiology is driven by the toxic overaccumulation of NAA in the brain. Chapter 2 shows that antisense oligonucleotide mediated knockdown of the NAA-synthesizing enzyme Nat8l lowers brain NAA and improves motor function and brain degeneration in CD mice. This work was published in *Annals of Neurology* in 2020.[25] Chapter 3 delves further into NAA overaccumulation, pinpointing the cell specific retention of NAA as a key component of Canavan disease dysfunction. This work, published in *Annals of Neurology* in 2021, demonstrates that constitutive deletion of the dicarboxylic acid transporter NaDC3, lowers brain NAA and prevents development of leukodystrophy and ataxia in Canavan disease mice. Finally, Chapter 4 addresses structural and functional alterations present in the Bergmann glia of Canavan disease mice, and contributions these changes might have to neuronal damage and the overall phenotype of CD. This work is

currently under review at *Glia*. Finally, concluding remarks will discuss the field of Canavan disease research as it stands today as well as future directions for therapeutic interventions.

CHAPTER 2 – ANTISENSE OLIGONUCLEOTIDE REVERSES LEUKODYSTROPHY AND IN CANAVAN DISEASE MICE

2.1 ABSTRACT

Marked elevation in the brain concentration of N-acetyl-L-aspartate (NAA) is a characteristic feature of Canavan disease, a vacuolar leukodystrophy resulting from deficiency of the oligodendroglial NAA cleaving enzyme aspartoacylase. We now demonstrate that inhibiting NAA synthesis by intracisternal administration of a locked nucleic acid antisense oligonucleotide to young adult aspartoacylase-deficient mice reverses their pre-existing ataxia and diminishes cerebellar and thalamic vacuolation and Purkinje cell dendritic atrophy.

2.2 INTRODUCTION

Canavan disease is a vacuolar leukodystrophy caused by ASPA gene mutations that block expression of functional aspartoacylase, an enzyme required for catabolism of the abundant brain amino acid N-acetyl-L-aspartate (NAA). Current therapies for Canavan disease, including dietary manipulations, lithium citrate administration, stem cell transplants, and brain intraparenchymal AAV-ASPA vector administration, have not been successful in reversing or preventing progression of Canavan disease.[17,18] The brain concentration of NAA ($[NAA_B]$) is markedly elevated in Canavan disease,[11,17] and also in aspartoacylase-deficient Canavan disease mice (CD mice). We now report that lowering $[NAA_B]$ in young adult CD mice by administration into cisterna magna of a locked nucleic acid antisense oligonucleotide (LNA-ASO, or "gapmer")[21,22,37–39] to knockdown expression of the neuronal NAA-synthesizing enzyme N-acetyltransferase 8-like (Nat8l)[40] reverses ataxia, Purkinje cell dendritic atrophy, and cerebellar/thalamic vacuolation.

2.3 MATERIALS AND METHODS

Mice heterozygous for the Aspa nonsense mutation $Aspa^{nur7}$ were obtained from the Jackson Laboratory (JAX:008607), maintained on a C57BL/6J background, and crossed to generate $Aspa^{nur7/nur7}$ CD mice[21,22] and age-matched $Aspa^{WT/WT}$ control mice (WT mice). An LNA-ASO[10] designed to knockdown Nat8l expression ("Nat8l gapmer", nucleotide sequence GGCGTAGAGCAGTTGG), and a negative control LNA-ASO without known eukaryote targets ("control gapmer", nucleotide sequence AACACGTCTATACGC), were from Qiagen, Inc., Germantown MD. Both gapmers were constructed with a phosphorothioate backbone and 2'-O-methoxyethyl-derivatized sugar modifications.[10] Nat8l or control gapmer (0.5nmol in 5µl of artificial CSF) was infused into the cisterna magna of 2 month old CD or WT mice at 1µl/minute under isoflurane anesthesia. No CD or WT mice died during this procedure, nor, with the exception of those sacrificed for brain harvest, did any die throughout the course of this study.

Accelerated rotarod testing (starting speed 4 RPM, increasing by 1.2 RPM every 10 seconds)[21] was performed by blinded observers. For biochemical and histological studies, mice were deeply anesthetized with ketamine/xylazine and perfused with cold PBS. After brain harvest, cerebella were dissected free, transected longitudinally, and cerebellar samples from each mouse were flash-frozen for Nat8l mRNA and NAA assays, or fixed in 4% paraformaldehyde in PBS, cryoprotected in 30% sucrose, and embedded in OCT prior to cryostat sectioning.Nat8l mRNA abundance was assayed by qRT/PCR,[21] normalized to Hsp90 mRNA abundance. NAA was assayed by high performance liquid chromatography (HPLC),[41] and expressed in □mol/gram cerebellar wet weight. Cerebellar cryostat sections were cut from the sagittal cerebellar midline at 10 µm (slide mounted) or 50 μm (free-floating) thickness for immunostaining. The 10 µm sections were incubated with rabbit anti-PLP1 (RRID:AB_2165785, 1:200) and mouse anti-QKI-7 (CC1) (RRID:AB_2173148, 1:100), and the 50µm sections were incubated with rabbit anti-calbindin (RRID:AB_868617, 1:200). For thalamic immunohistology, 10mm coronal cryostat

sections were cut between Bregma -1.06mm and -1.94mm, slide mounted, incubated with rabbit anti-PLP1 (RRID:AB_2165785, 1:200) and rat monoclonal anti-GFAP (gift of Dr. Virginia Lee, U. Penn, 1:300), then incubated with fluorescently-tagged secondary antibodies, counterstained with 4',6'-diamidino-2-phenylindole (DAPI), and imaged on a Nikon A1 laser scanning confocal microscope. Cerebellar white matter vacuoles were quantified using the NIS-Elements Annotate and Measure tool. Thalamic vacuoles and GFAP immunoreactivity were quantified in Imaris 9.3 (BitPlane) using 20x confocal z-stack images. Purkinje cell dendritic length and dendritic spine density were quantified in Imaris 9.3 using 60x confocal z-stack images. The Imaris Filament Tracing module was used to detect an automatic intensity threshold, subtract background noise, and generate dendrite computer reconstructions. Imaris parameters were set to detect dendritic spines between 0.2µm and 1.5µm in length. Purkinje cell dendritic total lengths were calculated by dividing total dendrite length/image by the number of Purkinje cell somas in the image. Images across treatment groups were analyzed with the same intensity thresholds. Statistical analyses were by one-way or two-way ANOVA with post-hoc Tukey test, or by 2-tailed Student's t-test. All animal experiments were conducted with UC Davis Institutional Animal Care and Use Committee approval, and in accordance with the United States Public Health Service's Policy on Humane Care and Use of Laboratory Animals.

2.4 RESULTS

Cerebellar Nat8l mRNA abundance was similar in untreated 2 month old CD and WT mice. Cerebellar Nat8l abundance was diminished in both CD and WT mice 2 weeks after intracisternal Nat8l gapmer administration, but had returned to pre-treatment levels by 2 months post-Nat8l gapmer (**Figure 2.1A**). Nat8l gapmer administration initially lowered [NAA_B] in CD mice, but not in WT mice. [NAA_B] reduction persisted in some, but not all, CD mice 2 months post-Nat8l gapmer (**Figure 2.1B**).

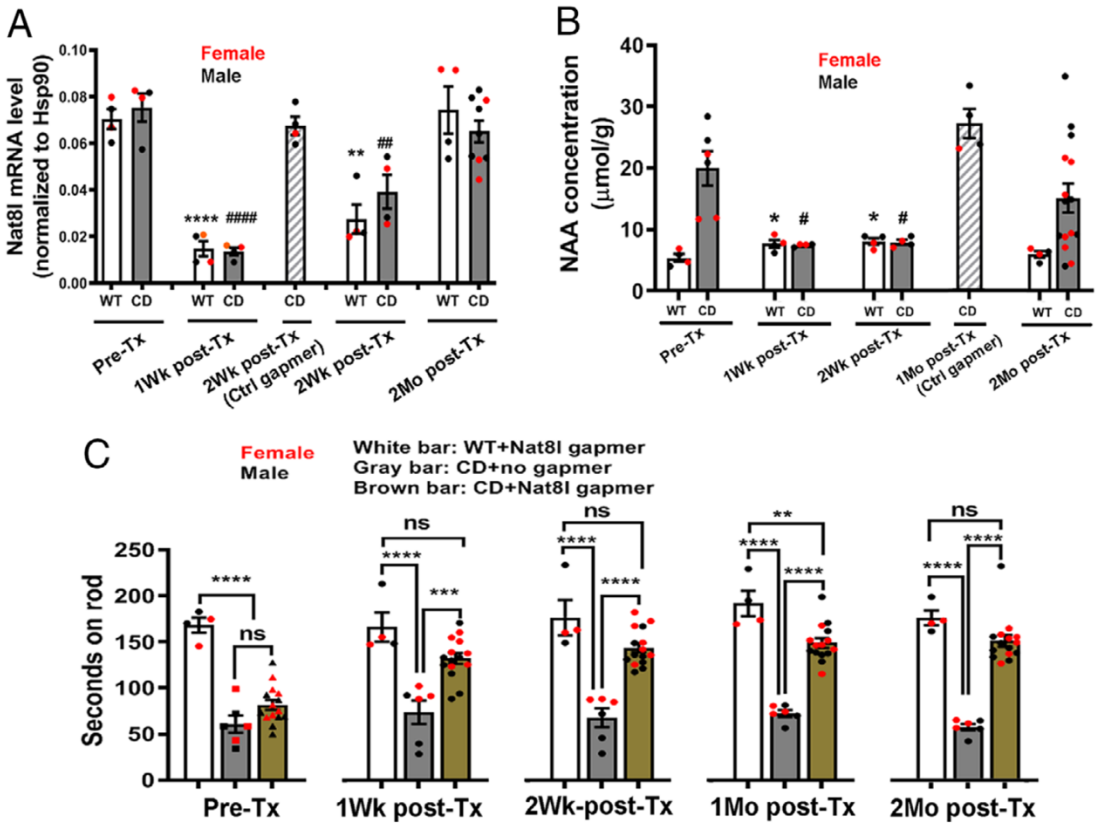

<u>Figure 2.1</u>: Effects of intracisternal *Nat8l* gapmer on cerebellar *Nat8l* mRNA abundance, [NAAB], and accelerating rotarod performance.
Each circle denotes data from an individual mouse (red female, black male). Means and SEMs are indicated. A) qRT/PCR for cerebellar Nat8l abundance. One way Anova, ####, 1 week post-treatment (post-Tx) CD different than pre-Tx CD, p< 0.0001; ****, 1 week post-Tx WT different than pre-Tx WT, p<0.001; **, ## and **, 2 week post-Tx WT and CD different than pre-Tx WT and CD, respectively, p<0.01. Control gapmer did not significantly alter Nat8l mRNA abundance in CD mice (striped bar). B) HPLC assays for NAA (in µmol/gram cerebellar wet weight). Kruskal-Wallis test. * and #, 1 and 2 wk post-Tx WT and CD different than pre-Tx WT and CD, respectively, p<0.05. Control gapmer did not significantly alter [NAAB] in CD mice (striped bar). C) accelerating rotarod retention times. ANOVA, ****, p<0.0001; ***, p<0.001; **, p<0.01. Accelerating rotarod performances of WT mice 2 weeks and 1 month post-intracisternal Nat8l gapmer (168.5+12.2, n=6, 3M/3F; and 199.1+12.8, n=6, 3M/3F, respectively) did not differ significantly from those of untreated WT mice of the same age. Accelerating rotarod performances of CD and WT mice 1 month post-control gapmer were not significantly different from those of untreated age- and sex-matched CD and WT mice, respectively (WT no treatment 173.5+8.3; treated WT 156.3+6.3, mean+SEM, n=4 mice/group, p=0.1493, two-tailed T test). Weight gains (in grams) during the interval between 2 and 4 months of age were not significantly different between untreated WT (4.4+0.7), untreated CD (4.1+0.3, Nat8l gapmer treated WT (5.5+1.8), and Nat8l gapmer treated CD (4.0+0.8) mice (p=0.7815, ANOVA). Two way ANOVA at each time-point indicated no significant differences between males and females.

Accelerating rotarod retention times in untreated 2 month old CD mice averaged less than half those in age-matched WT mice, but had increased significantly by 1 week post-Nat8l gapmer, and remained substantially above those in age-matched untreated CD mice 2 months post-Nat8l

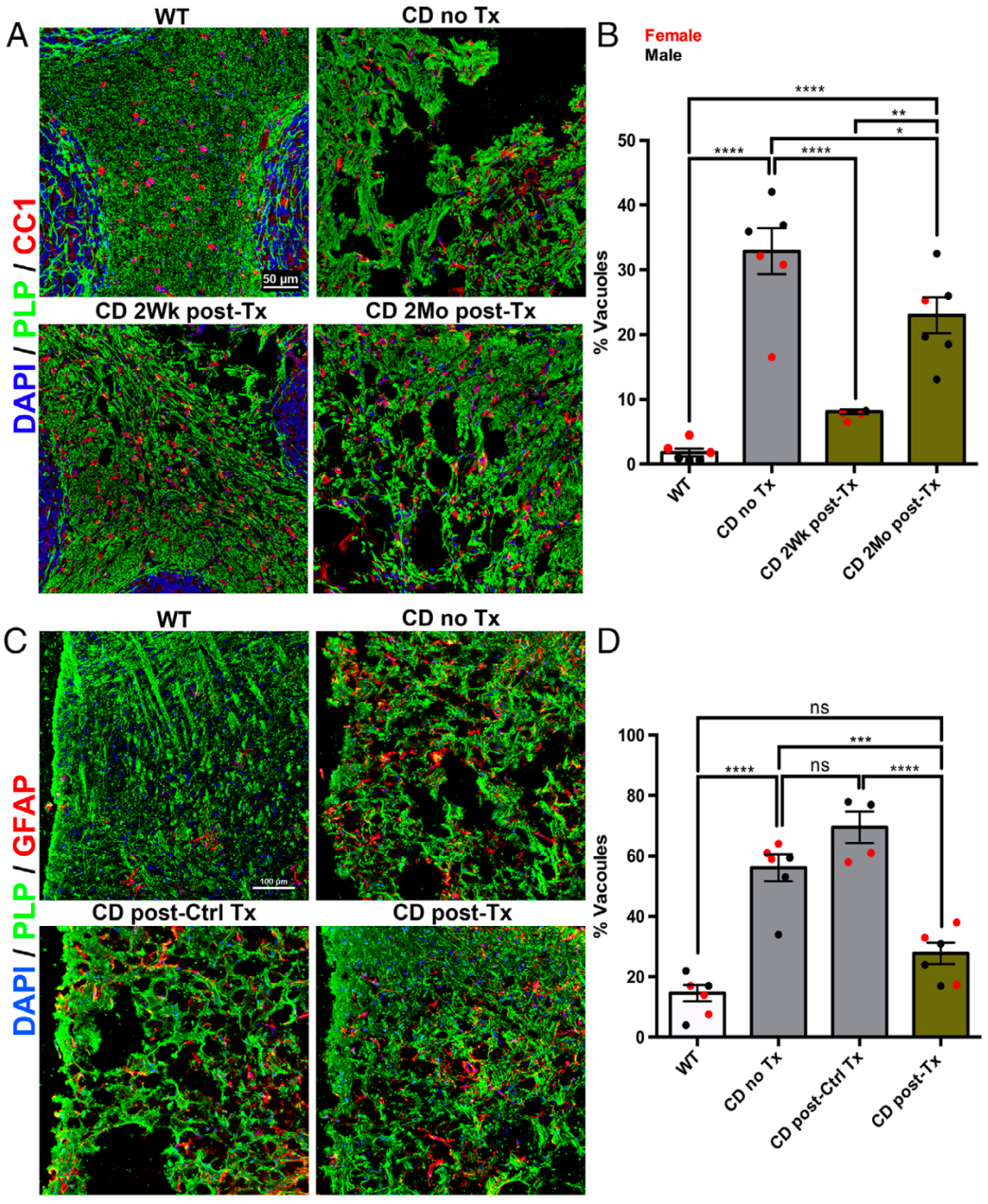

Figure 2.2: Effects of intracisternal Nat8l gapmer on cerebellar white matter vacuolation and oligodendroglial numbers and on thalamic vacuolation and GFAP immunoreactivity in CD mice. *(legend continued on next page)*

Figure 2.2: A) Images (z-stacks of four 2□m optical slices) immunostained for PLP and CC1, from representative WT, CD without Nat8l gapmer treatment (CD noTx), CD 2 weeks after Nat8l gapmer treatment (CD 2Wk post-Tx), and CD 2 months after Nat8l gapmer treatment (CD 2Mo post-Tx) mice. Size-bar 50□m in each panel. **B)** Cerebellar white matter vacuolar area; each circle represents an individual mouse. Means and SEMs (n=6 mice/group) are indicated. ****, p<0.0001; **, p<0.01, *, p<0.05, ANOVA. The effects of Nat8l gapmer treatment (Tx) on $CC1^+$ mature oligodendroglial numbers/mm^2 of cerebellar white matter (not corrected for white matter vacuolation) were: WT 330±28; CD noTx 300±36; CD 2Wk post-Tx 290± 12; and CD 2Mo post-Tx 340±48 (mean±SEM, n=3/group; one way ANOVA not significantly different). **C)** Images (z-stacks of 4 2mm optical slices), immunostained for PLP and GFAP, from representative 4 month old WT, CD noTx, CD 2 months post Ctrl Tx (CD post-Ctrl Tx) and CD 2 months post-Nat8l gapmer treatment (CD post-Tx). Size bar = 100mm in each panel. **D)** Thalamic vacuolar area; each circle represents an individual mouse. Means and SEMs (n=6 mice/group) are indicated. ****, p<0.0001; ***, p<0.001. Thalamic GFAP immunoreactivity (uncorrected for thalamic vacuole area, and expressed as % GFAP occupancy/field ± SEM) occupied 42.7±7.9% in 4 month old untreated CD mice; 2.92±0.52% in 4 month old wild-type mice; 33.3±4.5% in 4 month old control gapmer-treated mice; and 16.2±3.0% in 4 month old Nat8l gapmer-treated mice (n=4-6 mice, sex-matched/group). ANOVA with post hoc Tukey test indicated that GFAP immunoreactivity was more highly expressed in 4 month old untreated CD than WT mice (73457±13572 voxels vs 5016±898 voxels, mean±SEM, n=6, p<0.0001; and that there was no significant difference in GFAP immunoreactivity at age 4 months between CD mice that had received intracisternal Nat8l gapmer vs control gapmer at age 2 months (32620±2708 vs 57275±7667, mean±SEM, n=4, p=0.1851).

gapmer. The augmentative effect of Nat8l gapmer on CD mouse rotarod retention time was still present, but less marked, 3 months post-Nat8l gapmer (mean rotarod retention time 50.78 seconds in untreated CD mice vs 77.83 seconds in Nat8l gapmer-treated CD mice, p=0.0294; n=8 mice/group, 2-tailed t-test). Intracisternal administration of Nat8l gapmer or control gapmerdid not significantly alter accelerating rotarod retention times in WT mice, nor did intracisternal administration of control gapmer significantly alter accelerating rotarod retention times in CD mice (**Figure 2.1C**).

PLP immunostaining indicated that cerebellar white matter vacuolar area was diminished in CD mice sacrificed 2 weeks post-intracisternal Nat8l gapmer administration, and, to a lesser extent in CD mice sacrificed 2 months post-Nat8l gapmer. $CC1^+$ oligodendroglial numbers in cerebellar white matter (not corrected for vacuolation) were similar in 2 month old CD and WT mice, and, in CD mice, were not significantly altered by Nat8l gapmer administration (**Figure 2.2A,B**). Thalamic vacuole area was also diminished by Nat8l gapmer administration. Thalamic

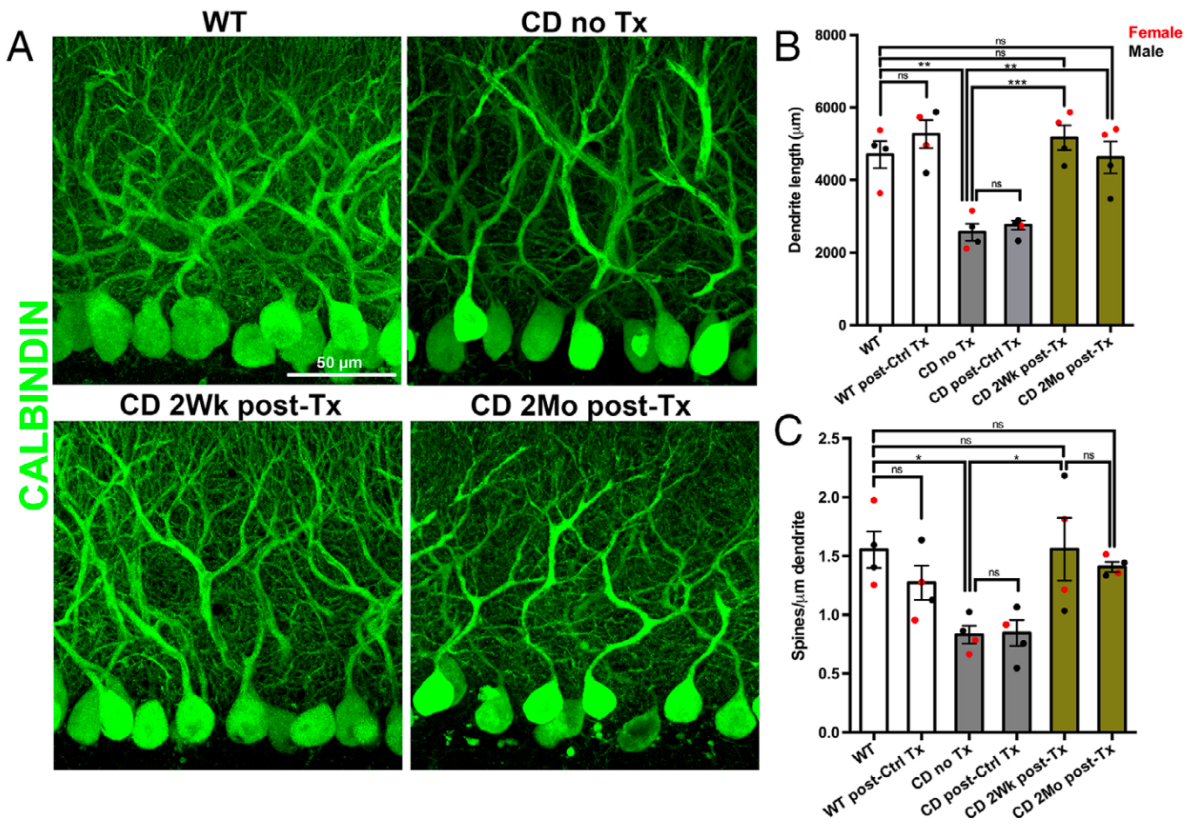

<u>Figure 2.3</u>: Effects of intracisternal Nat8l gapmer on Purkinje cell dendrite length and dendritic spine density in CD mice
A) Images (z-stacks of 30 1□m optical slices) from representative 4 month old WT, 4 month old CD without treatment (CD noTx), CD 2 weeks following Nat8l gapmer treatment at age 2 months (CD 2Wk post-Tx), and CD 2 months after Nat8l gapmer treatment at age 2 months (CD 2Mo post-Tx) mice. Size-bar = 50µm in each panel. B) Purkinje cell dendrite length; each circle denotes data from an individual mouse. Means and SEMs (n=4 mice/group) are indicated. ***, p<0.001; **, p<0.01; ANOVA. C) Purkinje cell dendritic spines/µm dendrite length; each circle denotes data from an individual mouse. Means and SEMs (n=6 mice/group) are indicated. *, p<0.05, ANOVA. Dendritic spines/mm dendrite length were not significantly more numerous in the CD 2Mo post-Nat8l gapmer Tx group than in either the CD no Tx or CD 2Mo post-Ctrl Tx groups, CD 2Mo post-Nat8l gapmer Tx group. However, dendritic spines/mm dendrite length were significantly higher in the 2 Mo post-Nat8l gapmer group than that in the combined 4 month old CD no Tx and CD 2 months post-Ctrl Tx groups (p=0.0354).e

immunoreactive GFAP (not corrected for vacuolation) was substantially greater in 4 month old CD than WT mice. Nat8l gapmer administration did not significantly diminish GFAP over-expression in CD mice **(Figure 2.2C,D**).

Purkinje cell dendrites were shorter and had fewer synaptic spines per unit length in 4 month old untreated CD than in 4 month old untreated WT mice. By 2 weeks post-Nat8l gapmer administration to 2 month old CD mice, Purkinje cell dendritic length and spines per unit dendritic

length were not significantly different than those in untreated 4 month old WT mice. The normalization of Purkinje cell dendritic length in the CD mice was still evident 2 months post-intracisternal Nat8l gapmer (**Figure 2.3**).

2.5 Discussion

Though early postnatal AAV-mediated ASPA gene therapy prevents leukodystrophy in CD mice,[42,43] attempts to translate ASPA gene therapy to infants and children with symptomatic Canavan disease have thus far failed to reverse pre-existing neurological deficits or to prevent disease progression.[17] Neonatal intracerebroventricular administration of an AAV incorporating a short hairpin Nat8l inhibitory RNA to CD mice, which lowered [NAA_B] toward normal, also prevented development of leukodystrophy.[24] However, a sharp decrease in brain transduction by the AAV vector after the newborn period precluded evaluation of the potential of this therapy to reverse pre-existing ataxia, cerebellar vacuolation, and alterations in Purkinje cell morphology in the CD mice.

Intrathecal administration of a single-stranded LNA-ASO for modification of neuronal SMN2 splicing is now in clinical use in infants and children with spinal muscular atrophy,[44] and other chemically modified oligonucleotides have shown therapeutic promise in suppressing synthesis of toxic neuronal proteins in animal models of human neurodegenerative diseases.[45] The present study demonstrates that inhibiting [NAA_B] elevation by intracisternal administration of an LNA-ASO designed to suppress expression of the neuronal NAA synthesizing enzyme Nat8l[40] rapidly reverses ataxia, Purkinje cell dendritic atrophy, and cerebellar and thalamic vacuolation in young adult CD mice. CD mouse cerebellar Nat8l mRNA abundance had returned to pretreatment levels by 2 months post-Nat8l gapmer, by which point [NAA_B] had already risen substantially, yet the marked improvement in accelerating rotarod performance of Nat8l gapmer-treated CD mice was fully maintained for 2 months, and was still substantially better than that in

untreated CD mice 3 months post-Nat8l gapmer. These therapeutic responses argue for consideration of intrathecal Nat8l gapmer therapy, either alone or as an adjunct to ASPA gene therapy, for infants and children with Canavan disease.

How might elevated [NAA_B] elicit vacuolation and Purkinje cell dendropathy? Raising [NAA_B] in aspartoacylase-expressing mice, for example by engineering neuronal transgenic Nat8l overexpression, does not alter brain histology.[46] However, several human and murine mutations that perturb expression of astroglial ion channel-associated proteins cause vacuolar leukodystrophies.[47] Since astroglia express a sodium-coupled plasma membrane dicarboxylic acid transporter with high affinity for NAA, NaDC3 (encoded by *Slc13a3)*[26], vacuolation in aspartoacylase-deficient brains may be attributable to the osmotic effects of astroglial NAA over-accumulation,[15,18] and the rapid therapeutic response to Nat8l gapmer may be attributable to restoration of normal astroglial NAA content and osmolar homeostasis. It is unclear whether the Purkinje cell dendritic abnormalities in young adult CD mice and the Purkinje cell losses previously reported in older CD mice[48] represent Purkinje cell-autonomous effects of elevated [NAA_B], or are secondary to astroglial or Bergmann cell dysfunction.

CHAPTER 3 – ABLATING THE SODIUM DICARBOXYLIC ACID TRANSPORTER NADC3 PREVENTS LEUKODYSTROPHY IN CANAVAN DISEASE MICE

3.1 ABSTRACT

Canavan disease is caused by *ASPA* mutations that diminish brain aspartoacylase activity, and is characterized by excessive brain storage of the aspartoacylase substrate N-acetyl-L-aspartate (NAA) and by astroglial and intramyelinic vacuolation. Astroglia and arachnoid mater express NaDC3, encoded by *Slc13a3*, a sodium-coupled transporter for NAA and other dicarboxylates. Constitutive *Slc13a3* deletion in aspartoacylase-deficient Canavan disease mice prevents brain NAA over-accumulation, ataxia, and brain vacuolation

3.2 INTRODUCTION

Canavan disease is a vacuolar leukodystrophy caused by *ASPA* mutations that diminish brain expression of aspartoacylase, an oligodendrocyte-enriched enzyme that cleaves the abundant brain amino acid N-acetyl-L-aspartate (NAA) to acetate and L-aspartate. The disease usually presents in infancy, with ataxia, hypotonia, and failure to acquire developmental milestones, often in association with macrocephaly, blindness, nystagmus, and seizures. Occasionally, the clinical onset is delayed until later in childhood.[113] Magnetic resonance imaging shows brain signal alterations indicative of cytotoxic edema and diffusion restriction;[25] proton magnetic resonance spectroscopy demonstrates a marked elevation in brain NAA concentration ($[NAA_B]$);[3] and neuropathological studies reveal “spongiform” vacuoles arising within myelin and astroglia.[46] No presently available therapies prevent or reverse Canavan disease.

$[NAA_B]$ is also elevated in mice homozygous for a nonsense *Aspa* mutation. These aspartoacylase-deficient “CD mice” develop central nervous system astroglial and intramyelinic vacuolation by postnatal day 14, and ataxia by postnatal day 21.[4] Suppressing $[NAA_B]$ elevation

by knocking out or knocking down *Nat8l*, which encodes the neuronal NAA synthesizing enzyme N-acetyltransferase 8-like (N-acetylaspartate synthase), prevents ataxia and brain vacuolation in these mice,[21,25,39] thus supporting the hypothesis that leukodystrophy in aspartoacylase-deficient brains is a consequence of brain NAA overload.

The Na^+/dicarboxylate cotransporter NaDC3, encoded by *Slc13a3*, a member of the *Slc13* Na^+-coupled di- and tri-carboxylate/sulfate transporter gene family, provides the only thus far established means by which mammalian cells can import NAA. [26,27,49] The present study surveys murine brain *Slc13a3* mRNA and immunoreactive NaDC3 expression, and evaluates the phenotypic consequences of constitutive *Slc13a3* deletion (*Slc13a3*$^{KO/KO}$) in aspartoacylase-expressing (*Aspa*$^{WT/WT}$) and CD (*Aspa*$^{Nur7/Nur7}$) mice.

3.3 MATERIALS AND METHODS

Mice heterozygous for the *Aspa*^{nur7} nonsense mutation were obtained from the Jackson Laboratory (JAX:008607; Bar Harbor, ME). Heterozygous constitutive *Slc13a3*^{KO} mice were obtained from the MMRRC (MMRRC:049666-UCD; UC Davis). These two strains were crossed to obtain *Aspa*$^{nur7/nur7}$/*Slc13a3*$^{KO/KO}$ and *Aspa*$^{nur7/nur7}$/*Slc13a*$^{WT/KO}$ mice, referred to hereafter as CD/*Slc13a3*$^{KO/KO}$ and CD/*Slc13a3*$^{WT/KO}$ mice respectively. *Aspa*$^{WT/WT}$/*Slc13a3*$^{WT/WT}$ and CD/*Slc13a3*$^{WT/WT}$ mice were from the same mouse colony. *Prox1*-tdTomato transgenic *Prox1* reporter (*Prox1-TdTomato*) mice were from the Jackson Laboratory (JAX:018128).[50] Mice were maintained on a C57BL/6 background in an AAALAC-certified vivarium, and mouse protocols were conducted in accordance with the USPHS Policy on Humane Care and Use of Laboratory Animals.

Accelerating rotarod testing (starting speed 4 RPM, increasing by 1.2 RPM every 10 seconds) was performed by blinded observers. Urine was collected from the mice on postnatal day 60 (p60), and was treated with 0.1M KH_2PO_4 and 0.1M KCl, pH 3.75, and filtered. The eluate

underwent liquid-liquid phase separation with acetonitrile, cyclohexanone, diethyl ether, and chloroform. The aqueous layer was collected for HPLC analysis as previously described.[25]

For biochemical and histological studies, mice were deeply anesthetized with ketamine/xylazine and perfused with cold phosphate-buffered saline. Forebrain, cerebellar, spinal cord, and kidney sections were flash-frozen in liquid nitrogen for mRNA, protein, and NAA assays.[25] For immunohistology, samples of forebrain and cerebellum were postfixed in 4% paraformaldehyde in PBS, cryoprotected in 30% sucrose, embedded in OCT compound, and frozen. Cryostat sections were immunostained for NaDC3 (RRID AB_2868533), vimentin (RRID AB_10003206), MBP (RRID AB_10655672), GFAP (gift from V. Lee, U. Penn.), or collagen 1a1 (RRID AB_10891543), counterstained with DAPI, and imaged on a Nikon A1 laser scanning confocal microscope. Cerebellar and thalamic white matter vacuole areas were measured using the NIS-Elements Annotate and Measure tool (Nikon).[25]

Mixed glial cell preparations were prepared from forebrains of P0 to P2 mouse pups, used to prepare astroglia-enriched cultures (92% $\pm$ 2% $GFAP^+$; n=3, mean $\pm$ SEM) by differential shaking. Samples of kidney, cerebellum, microdissected forebrain meninges and choroid plexus,[51] and harvested astroglia-enriched cultures, were assayed for mRNAs by quantitative RT/PCR. Primer pairs were as previously described,[52] with the exception that primer pairs for *Slc13a3* were: forward 5'-CTAGGAGGTGGCTTTGCC-3'; and reverse 5'-ACTCCGTGAAGAAGGCGATG-3'. Quantitative RT/PCR results were normalized to *Hsp90* mRNA abundance. Cerebellar NAA content was assayed by high-performance liquid chromatography and expressed in mm/gram tissue wet weight.[25] Quantitative data are presented in the figures as means $\pm$ standard errors, and statistical analyses were by one- and two-way ANOVA with post-hoc Tukey test.

3.4 RESULTS

Figure 3.1 quantifies and localizes brain *Slc13a3*/NaDC3 expression in *Aspa*$^{WT/WT}$ mice. We confirmed a prior report that cultured astroglia express *Slc13a3* mRNA,[1127f] and, in cryostat sections of adult murine forebrain, detected faint NaDC3 immunoreactivity in GFAP^{+} astroglia, but not in other parenchymal cells. *Slc13a3* mRNA abundance in adult mouse forebrain meninges was 20-fold higher than in mouse astroglial cultures. Immunoreactive NaDC3 in the meninges was confined to arachnoid mater, and, in *Prox1-TdTomato Prox1* reporter mice, was expressed by arachnoid cells that were co-labelled with TdTomato.

Figure 3,2 demonstrates a lack of effects of homozygous constitutive *Slc13a3* disruption (*Slc13a3*$^{KO/KO}$) on cerebellar myelination in *Aspa*$^{WT/WT}$ mice. Between postnatal day 7 (p7) and p60, cerebellar levels of immunoreactive PDGFRa, Sox10, TCF7L2, MAG, and MBP proteins in *Aspa*$^{WT/WT}$/*Slc13a3*$^{KO/KO}$ mice did not differ significantly from those in *Aspa*$^{WT/WT}$/*Slc13a3*$^{WT/WT}$ mice, and patterns of p60 cerebellar MBP immunostaining in *Aspa*$^{WT/WT}$/*Slc13a3*$^{KO/KO}$ and *Aspa*$^{WT/WT}$/*Slc13a3*$^{WT/WT}$ mice were indistinguishable. Also between p7 and p60, there were no significant differences between *Aspa*$^{WT/WT}$/*Slc13a3*$^{KO/KO}$ and *Aspa*$^{WT/WT}$/*Slc13a3*$^{WT/WT}$ mice in spinal cord abundances of *Nat8l*, *Gfap*, *Pdgfra*, *Tcf7l2*, *Mag*, and *Mbp* mRNAs. In fact, the only phenotypic effect of constitutive *Slc13a3*$^{KO/KO}$ we detected in *Aspa*$^{WT/WT}$ mice was a substantial elevation in urinary NAA concentration (Figure 3A).

Figure 3.3 describes the effects of *Slc13a3*$^{KO/KO}$ in CD mice. Urinary NAA concentrations, already elevated in the CD/*Slc13a3*$^{WT/WT}$ mice, were substantially further increased in CD/*Slc13a3*$^{KO/KO}$ mice (Figure 3.3A). Notably, *Slc13a3*$^{KO/KO}$, though not altering *Nat8l* mRNA abundance in the CD mice, normalized [NAA_B], increased their weight at p60 and their accelerating rotarod retention times, and prevented cerebellar and thalamic vacuolation. Heterozygous *Slc13a3* deletion in CD mice also suppressed [NAA_B] elevation, enhanced accelerating rotarod performance, and partially prevented cerebellar but not thalamic vacuolation.

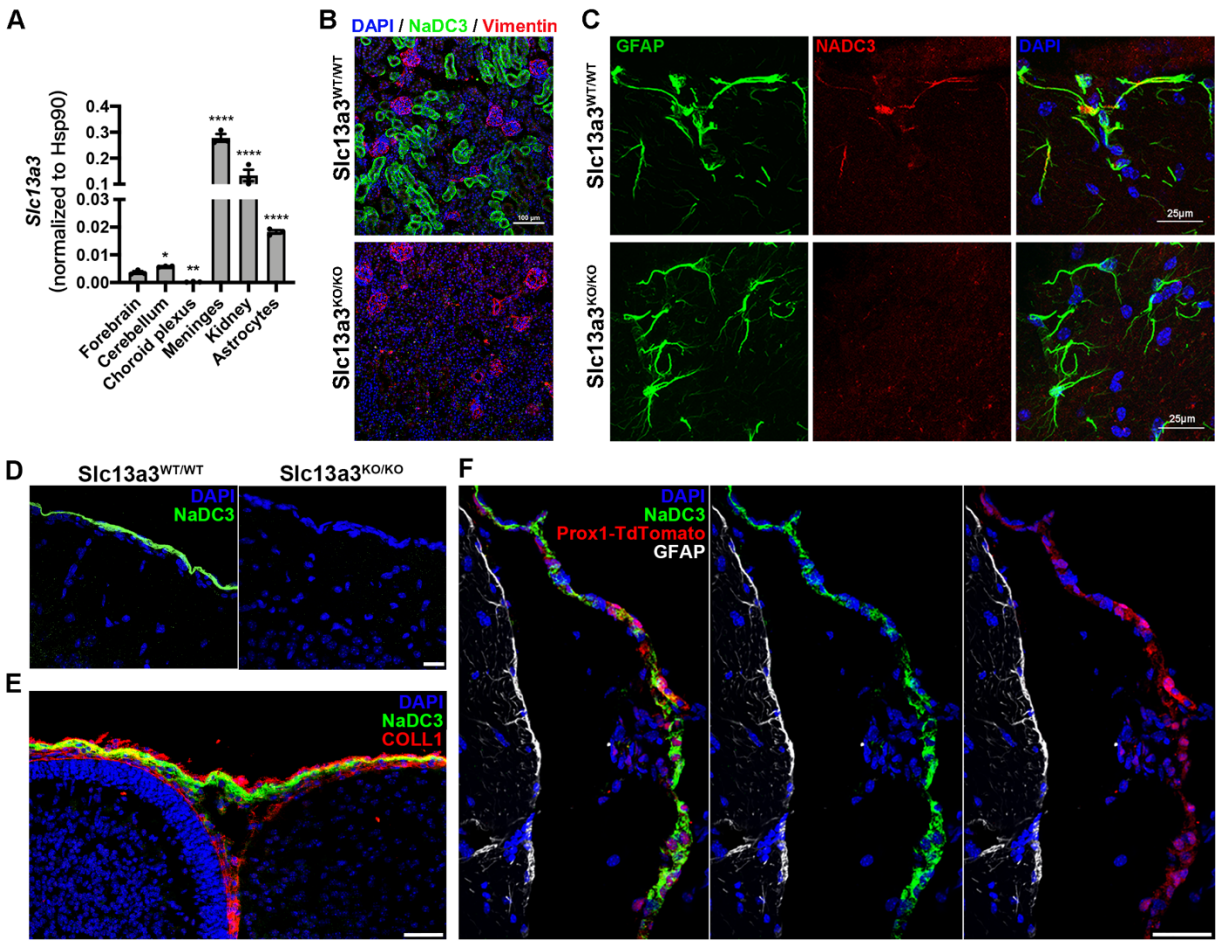

Figure 3.1: Comparison of the renal and brain *Slc13a3* mRNA and NaDC3 expression between *Slc13a3*$^{WT/WT}$ and *Slc13a3*$^{KO/KO}$ mice.

Panel A -- *Slc13a3* mRNA abundance in homogenates prepared from adult forebrain and cerebellar parenchyma, micro-dissected adult forebrain meninges and choroid plexus, adult mouse kidney, and cultured neonatal mouse astrocyte-enriched cultures. Results are means of determinations from 3 mice or 3 cultures, with vertical lines indicating SEMs. *p<0.05; **p<0.01; ****P<0.0001. Panel B - Renal tubular NaDC3 immunostaining (green) was detected in *Aspa*$^{WT/WT}$/*Slc13a3*$^{WT/WT}$ mice, but not in *Aspa*$^{WT/WT}$/*Slc13a3*$^{KO/KO}$ mice; glomeruli were vimentin^{+} (red) and nuclei were stained with DAPI (blue); scale bar = 100mm. Panel C - Some GFAP^{+} astroglia in adult forebrain parenchyma of *Aspa*$^{WT/WT}$/*Slc13a3*$^{WT/WT}$ mice expressed immunoreactive NaDC3, but immunoreactive NaDC3 was not detected in astroglia of *Aspa*$^{WT/WT}$/*Slc13a3*$^{KO/KO}$ mice; scale bar = 25mm. Panel D - Meningeal immunoreactive NaDC3 was detected in adult *Aspa*$^{WT/WT}$/*Slc13a3*$^{WT/WT}$ mice, but not in *Aspa*$^{WT/WT}$/*Slc13a3*$^{KO/KO}$ mice. Panel E - Immunoreactive NaDC3 was detected in cerebellar arachnoid mater of neonatal *Aspa*$^{WT/WT}$/*Slc13a3*$^{WT/WT}$ mice, lying below collagen 1a1^{+} immunoreactive cells in dura and above collagen1a1^{+} immunoreactive cells in pia. Panel F - NaDC3 (green) and *Prox1* reporter TdTomato (red) immunoreactivities were co-localized in forebrain arachnoid mater of adult *Aspa*$^{WT/WT}$/*Slc13a3*$^{WT/WT}$ mice; GFAP^{+} (white) glia limitans is on the left in the panel. Scale bar in D-F = 50mm. Each of the microscopic fields shown in Panels B-F is representative of results from at least 3 individual adult or neonatal mice.

Abundances of cerebellar oligodendroglial lineage mRNAs did not differ significantly between *Aspa*$^{WT/WT}$/*Slc13a3*$^{WT/WT}$, *Aspa*$^{WT/WT}$/*Slc13a3*$^{KO/KO}$, CD/*Slc13a*3$^{WT/WT}$, and CD/*Slc13a3*$^{KO/KO}$ mice.

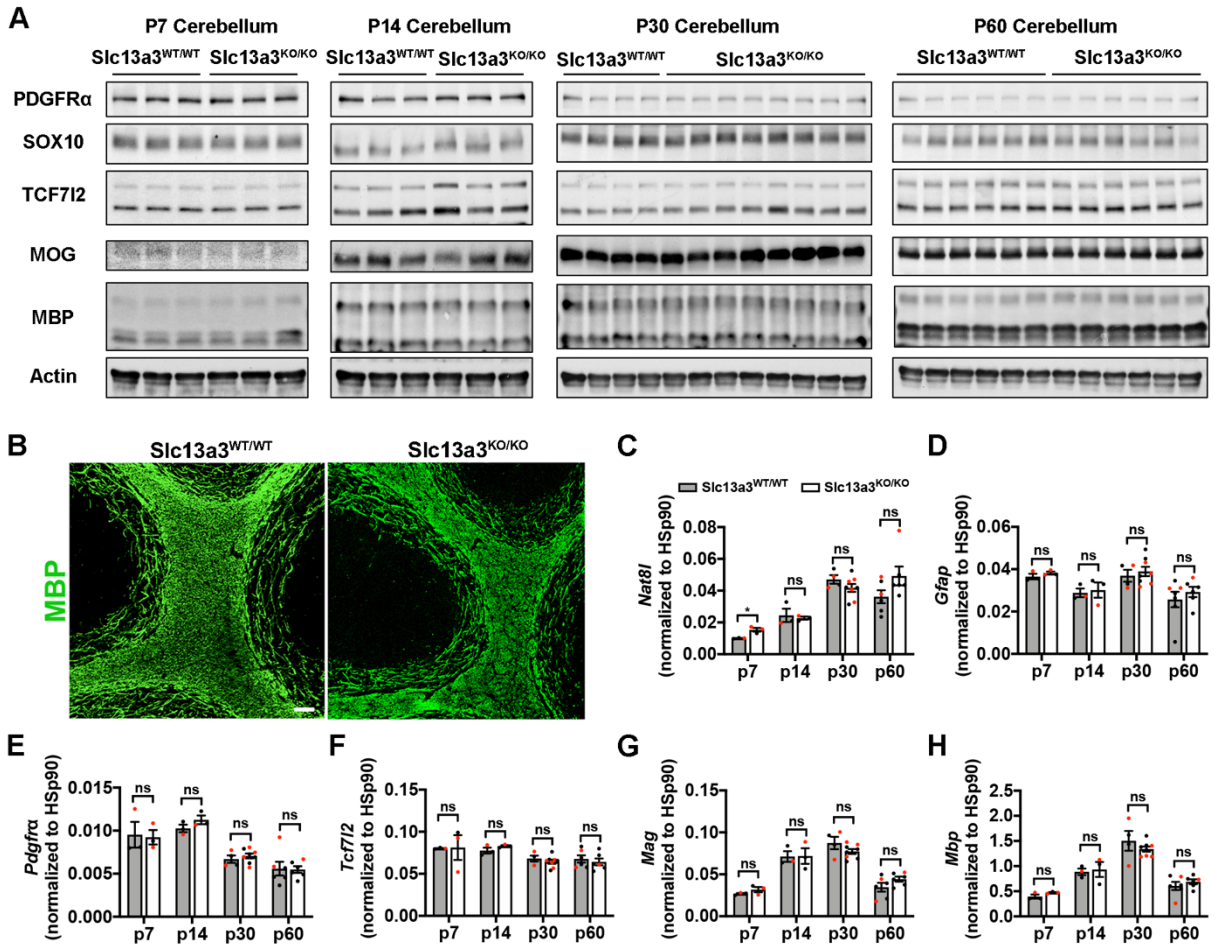

Figure 3.2: Constitutive *Slc13a3*$^{KO/KO}$ does not alter expression levels of myelin proteins in AspaWT/WT cerebellum between p7 and p60, nor alter p7-p60 abundances of neuronal (*Nat8l*), astroglial (*Gfap*), or oligodendroglial lineage (*Pdgfra*, *Tcf7l2*, *Mag*, *Mbp*) marker mRNAs in AspaWT/WT spinal cord.

Panel A - Western blots of oligodendroglial lineage/myelin protein levels in cerebellar homogenates of *Aspa*$^{WT/WT}$/*Slc13a3*$^{WT/WT}$ and *Aspa*$^{WT/WT}$/*Slc13a3*$^{KO/KO}$ mice on p7, p14, p30, and p60; Western blot lanes from 3 mice of each genotype are shown at each time-point. Panel B - Patterns of MBP immunostaining were similar in cerebella of p60 *Aspa*$^{WT/WT}$/*Slc13a3*$^{WT/WT}$ and *Aspa*$^{WT/WT}$/*Slc13a3*$^{KO/KO}$ mice; scale bar = 50mm. Panels C-H -- Abundances (assayed by qRT/PCR) of *Nat8l*, *Gfap*, *Pdgfra*, *Tcf7l2*, *Mag*, and *Mbp* mRNAs in spinal cord homogenates prepared from *Aspa*$^{WT/WT}$/*Slc13a3*$^{WT/WT}$ and *Aspa*$^{WT/WT}$/*Slc13a3*$^{KO/KO}$ mice on p7, p14, p30, and p60. Each dot (red = female; black = male) in Panels C-H represents an individual mouse. The height of each column indicates the mean, and the vertical lines indicate SEMs. “ns” = non-significant differences between the two genotypes at each time-point.

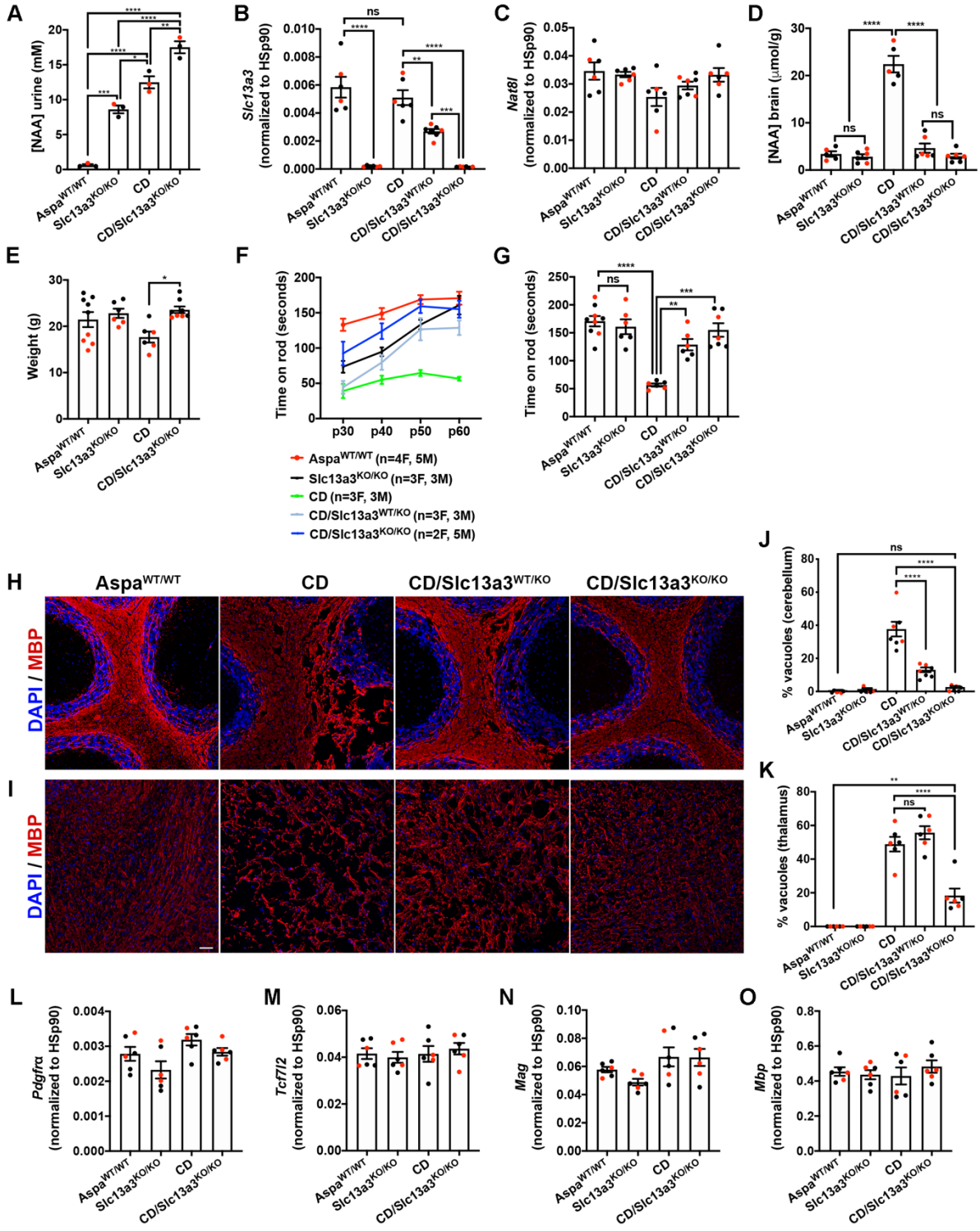

Figure 3.3: Constitutive *Slc13a3*$^{KO/KO}$ increases urinary NAA output, normalizes [NAAB], enhances weight gain and rotarod performance, and prevents brain vacuolation in CD mice.
(legend continued on next page)

Figure 3.3: *(Continued from last page)* Panel A – Additive effects of CD genotype and *Slc13a3*$^{KO/KO}$ on urinary NAA concentration ($[NAA]_{urine}$). Panel B – *Slc13a3* mRNA abundances in *Aspa*$^{WT/WT}$/*Slc13a3*$^{WT/WT}$, *Aspa*$^{WT/WT}$/*Slc13a3*$^{KO/KO}$, CD/*Slc13a3*$^{WT/WT}$ (CD), CD/*Slc13a3*$^{WT/KO}$, and CD/*Slc13a3*$^{KO/KO}$ brains. Panel C – No significant effects of *Slc13a3*$^{KO/KO}$ on *Nat8l* mRNA abundance in *Aspa*$^{WT/WT}$ or CD brains. Panel D - - *Slc13a3*$^{KO/KO}$ did not alter [NAA_B] in *Aspa*$^{WT/WT}$ brains, but either *Slc13a3*$^{KO/KO}$ or *Slc13a3*$^{WT/KO}$ normalized [NAA_B] in CD brains. Panel E – Body weights were higher in p60 CD/*Slc13a3*$^{KO/KO}$ mice than in p60 CD mice. Panels F and G - *Slc13a3*$^{KO/KO}$ enhanced accelerating rotarod retention times in CD mice, but not in *Aspa*$^{WT/WT}$ mice; the results at p60 are shown in more detail in Panel G. Panels H and J - *Slc13a3*$^{KO/KO}$ prevented, and *Slc13a3*$^{WT/KO}$ diminished, cerebellar vacuolation in p60 CD mice. Panels I and K - *Slc13a3*$^{KO/KO}$ prevented thalamic vacuolation in p60 CD mice, but *Slc13a3*$^{WT/KO}$ did not. Microscopic fields shown in Panels H and I are representative of those in 6 mice in each group. Panels L-O - *Slc13a3*$^{KO/KO}$ did not significantly alter cerebellar abundances of *Pdgfra*, *Tcf7l2*, *Mag*, or *Mbp* mRNA in p60 CD mice. In Panels A-E, G, and J-O, each dot (red = female; black = male) represents an individual mouse. Analysis of the data in A-D, G, and J-O revealed no significant differences between males and females, but analysis of the data in Panel E indicated that males weighed more than females at p60, and that *Slc13a3*$^{KO/KO}$ increased rotarod retention times in both male and female CD mice ($p<0.05$ for each sex). Column heights indicate means, and vertical lines indicate SEMs. *p<0.05; **p<0.01; ***p<0.001; ****P<0.0001. Scale bar in I, J = 50mm.

3.5 DISCUSSION

Almost all NAA in normal brains is stored within neurons.[53] Where the additional NAA in Canavan disease and CD mouse brains accumulates has not yet been established, but the prominent astroglial vacuolation in aspartoacylase-deficient brains suggests that at least some of this additional NAA becomes sequestered within and, in conjunction with co-transported Na^+, perturbs osmolar homeostasis of NaDC3-expressing astroglia. If so, then [NAA_B] normalization and prevention of vacuolation in CD mice by constitutive *Slc13a3*$^{KO/KO}$ may represent the combined effects of accelerated brain export of non-neuronal NAA that was prevented from entering astroglia by astroglial NaDC3 ablation and enhanced renal NAA excretion owing to deletion of renal proximal tubular NaDC3.

Meningeal lymphatic vessels are a major route of cerebrospinal fluid (CSF) drainage from the brain,[54] and lymphatic endothelial cells can be identified by their expression of the transcription factor Prox1.[55] By analogy with the kidney, in which tubular epithelial cell NaDC3 limits urinary excretion of NAA, a-ketoglutarate, and other dicarboxylates, [30,49]resorption of NAA from the CSF by $Prox1^+$/$NaDC3^+$ arachnoid cells may contribute to [NAA_B] elevation in CD mice. *Slc13a3*

conditional deletion studies would permit evaluation of the respective contributions of astroglial and arachnoidal NaDC3 ablation in suppressing this [NAA_B] elevation.

Gene therapies to prevent leukodystrophy in CD mice by driving brain expression of functional aspartoacylase are already available, [43,56] but have not yet been successfully scaled up to human brains.[3] Development of a druggable *Slc13a3* or NaDC3 inhibitor might provide a more readily translatable therapeutic approach than gene therapy for infants and children with Canavan disease. Such an inhibitor would probably not adversely affect developmental brain myelination, since myelination in *Slc13a3*$^{KO/KO}$ mice did not differ significantly in time-course from that in *Slc13a3*$^{WT/WT}$ mice. A prior study demonstrating that lowering [NAA_B] in young adult CD mice by intracisternal administration of an *Nat8l* antisense oligonucleotide temporarily reversed established brain vacuolation and motor deficits[8] suggests that such an *Slc13a3* or NaDC3 inhibitor could be beneficial in already symptomatic Canavan disease children. A cautionary note, however, is that, although *Slc13a3*$^{KO/KO}$ was well tolerated in *Aspa*$^{+/+}$ and CD mice, a recent publication described two unrelated children with *SLC13A3* mutations limiting NaDC3 activity who presented with acute reversible episodes of leukoencephalopathy triggered by infections.[30]

CHAPTER 4 – PATHOLOGICAL BERGMANN GLIA ALTERATIONS AND DISRUPTED CALCIUM DYNAMICS IN ATAXIC CANAVAN DISEASE MICE

4.1 ABSTRACT

Canavan disease (CD) is a recessively-inherited pediatric leukodystrophy resulting from inactivating mutations to the oligodendroglial enzyme aspartoacylase (ASPA). ASPA is responsible for hydrolyzing the amino acid derivative N-acetyl-L-aspartate (NAA), and without it, brain NAA concentrations increase by 50% or more. Infants and children with CD present with progressive cognitive and motor delays, cytotoxic edema, astroglial vacuolation and prominent spongiform brain degeneration. ASPA-deficient CD mice (*Aspa*$^{nur7/nur7}$) similarly present with elevated NAA, vacuolar leukodystrophy, ataxia, and, as we have recently reported, Purkinje cell (PC) dendritic simplification and spine loss. Bergmann glia (BG), radial astrocytes integral for cerebellar development, are intimately intertwined with PCs, where they regulate synapse stability, functionality and plasticity. BG damage is common to many neurodegenerative conditions and frequently associated with PC dysfunction and ataxia. Here, we report that, in CD mice, BG exhibit significant structural alterations, decreased PC interactions and synaptic markers, depletion of glutamate transporters and Ca^{2+}-permeable AMPARs and altered calcium dynamics. We previously developed an antisense oligonucleotide (ASO) therapy targeting Nat8l (N-acetyltransferase-8-like, “Nat8l ASO”) that inhibits the production of NAA and reverses ataxia and PC atrophy in CD mice. Here, we show that Nat8l ASO administration in adult CD mice also leads to BG repair, suggesting that restoration of BG structural and functional integrity is a mechanism for PC regeneration and improved motor function.

4.2 INTRODUCTION

Aspa mutations disrupting the function of the oligodendroglial-enriched enzyme aspartoacylase (ASPA) cause Canavan disease (CD), a neurodegenerative leukodystrophy [9]. Without ASPA-mediated cleavage of the abundant brain metabolite N-acetyl-L-aspartate (NAA), brain NAA becomes markedly elevated in CD patients [4,11]. Infants and children with CD exhibit profound impairments in cognitive and motor function, cytotoxic edema, vacuolar brain degeneration and astrogliosis [57,58]. CD mice (*Aspa*$^{nur7/nur7}$) present with similarly elevated NAA, spongiform leukodystrophy, ataxia and Purkinje cell (PC) damage [22,25]. Here, we demonstrate striking structural and functional alterations to Bergmann glia (BG) in CD mice, as well as disturbed BG-PC interactions.

BG, the radial astrocytes of the cerebellum, direct the cytoarchitectural and functional development of the cerebellum and continue to support neuronal survival and synaptic function in adulthood. These specialized cells maintain their unipolar morphology throughout development, extending processes that traverse the entire molecular layer, terminating in subpial endfeet that form the cerebellar glial limitans [59–62]. BG are instrumental in the cytoarchitectural development of the cerebellum, much like the radial glial cells of the cerebral cortex [63], with their long fibers acting as a scaffold that guides the migration of the dense excitatory granule cell (GC) population to their final destination [60,64]. BG also regulate the complex dendritic arborization of the PCs [34,35], inhibitory neurons that project to deep cerebellar nuclei and represent the sole motor output of the cerebellum.

During synaptogenesis, the previously smooth BG fibers form lateral projections that surround developing synapses in the molecular layer, forming glial microdomains [65]. BG microdomains will eventually enwrap both parallel fiber (PF)-PC synapses, which are the axonal inputs from the GCs, and climbing fiber (CF)-PC synapses [62]. The combined input from PFs and CFs modulates the inhibitory output of the PCs which, in turn, influences motor coordination,

motor control and learning [66]. BG microdomains facilitate rapid glutamate reuptake (Storck et al., 1992; Bergles, Dzubay and Jahr, 1997) mediated by glutamate transporters GLAST (glutamate aspartate transporter 1) and GLT1 (glutamate transporter 1) [67–70]. BG also regulate ion homeostasis [71] and sense and respond to both excitatory and inhibitory neurotransmission, via expression of Ca^{2+}-permeable AMPARs [72,73], and $GABA_A$ receptors [74,75]. Like all astrocytes, BG exhibit intracellular calcium fluctuations that can be spontaneous or evoked by synaptic activity [65,76]. Stimulation of PFs and/or CFs produces localized calcium transients in BG microdomains [65,76–78].

Multiple animal models of BG ablation present with dysregulation of cerebellar neuronal migration, abnormal PC arborization, loss of motor coordination and ataxia [79,80], underscoring the vital role BG play in cerebellar development, information processing and functional output [66]. PCs are also particularly susceptible to damage in cerebellar ataxias and recent studies show that BG alterations often accompany, and may even precede, PC damage (see Cerrato, 2020 for a comprehensive review of this topic). Here, in addition to describing complex alterations to BG and BG-PC interactions in CD mice, we also show improvements to BG phenotypes after intracisternal delivery of an antisense oligonucleotide (ASO) previously reported by our lab to lower brain NAA and reverse leukodystrophy, ataxia and PC damage in CD mice ("Nat8l ASO").[25]

4.3 METHODS

Mice

Mice heterozygous for the *Aspa*^{nur7} nonsense mutation (RRID:IMSR_JAX:008607) were maintained on a C57Bl/6J background and crossbred to generate *Aspa*$^{nur7/nur7}$ "CD mice" and sex and age-matched *Aspa*$^{WT/WT}$ controls ("WT mice"). Aldh1L1-eGFP mice were also obtained from Jackson Laboratory (RRID:IMSR_JAX:030247) and crossbred to generate Aldh1L1-

eGFP/*Aspa*$^{nur7/nur7}$ CD mice and sex and age-matched Aldh1L1-eGFP/*Aspa*$^{WT/WT}$ controls. For tissue harvest, mice were deeply anesthetized with ketamine/xylazine and transcardially perfused with cold phosphate-buffered saline. Cerebella were bisected sagittally and half was flash frozen for mRNA and biochemical assays and half was postfixed in 4% paraformaldehyde (PFA) in PBS, cryoprotected and embedded in optimal cutting temperature (OCT) compound and frozen. All animal experiments were conducted with the approval of the Institutional Animal Care and Use Committee of the University of California, Davis.

Rotarod

Accelerating rotarod testing (4 rpm starting speed, increasing by 1.2 rpm every 10 seconds) was performed by blinded observers. Each data point represents the average score for an individual mouse over 9 trials.

qRT/PCR

Total mRNA was isolated from cerebellar samples and assayed by quantitative RT/PCR. Results were normalized to Hsp90 mRNA abundance. Primer pairs detailed in Table 4.1.

Immunohistochemistry and image analysis

OCT embedded, frozen cerebella were cryosectioned at 14 µm (slide mounted) or 50 µm (freefloating) and immunostained. Sections were incubated with primary antibodies (see Table 1) then incubated with secondary antibodies conjugated with fluorescent labels and counterstained with 4',6-diamidino-2-phenylindole (DAPI) (Primary antibodies detailed in Table 1). All imaging was done on a Nikon C2 laser scanning confocal microscope and consistent laser settings were used for all WT vs CD comparative images. Image analyses were performed in NIS-Elements (vacuolation quantification) or Imaris 9.7 (Bitplane, Zürich, Switzerland). Imaris was used to quantify BG process features (filament tracer), BG volume (surface tool), BG-PC proximity (surface tool with proximity filtering), VGLUT1 mean fluorescence intensity (surface tool) and

VGLUT2 puncta per PC (spots tool). Except in the case of Aldh1L1-eGFP/vimentin volume quantification, ROIs excluded the molecular layer and PC layer.

Calcium imaging

Mice (postnatal day p20-p30) were deeply anesthetized with ketamine/xylazine and cerebella were vibratome-sectioned at 250 µm ice cold-cutting solution. Cutting solution consisted of 75 mM sucrose, 87 mM NaCl, 25 mM Glucose, 25 mM $NaHCO_3$, 7 mM $MgCl_2$, 2.5 mM KCl, 1.25 mM NaH_2PO_4, 0.5 mM $CaCl_2$, bubbled with 5% CO_2/95%O_2. Slices were then incubated in sulforhodamine 101 (SR101, Invitrogen) in artificial cerebrospinal fluid (aCSF) for 20 minutes, followed by aCSF alone for 10 minutes, both at 34°C bubbling with 5% CO_2/95%O_2. aCSF solution consisted of 125 mM NaCl, 25 mM Glucose, 25 mM $NaHCO_3$, 7 mM $MgCl_2$, 2.5 mM KCl, 1.25 NaH_2PO_4, and 2 mM $CaCl_2$: ~300 mOsm. Slices were then incubated in 5µM Fluo4-AM (ThermoFisher Scientific) in aCSF at room temperature for 45 minutes, then washed in aCSF before being time-lapse imaged by a Swept-Field confocal microscope (Nikon) at an acquisition rate of 5 Hz for 5 minutes. For treated slices, 0.3 µm AMPA was added just prior to image acquisition. Videos were analyzed using NIS Elements. Fluorescence intensity (AU) for sample traces was quantified as $\Delta F/F_0$ with F_0 being average baseline intensity. Number of transients per minute over a 5-min recording window in an 1000 μm^3 ROI were averaged for each animal so that each data point represents the average of 3 ROIs (each from a different slice) for 1 animal. Duration of transients are reported in seconds (s) with each data point representing the average transient duration or rise time duration during a 5-min recording window in a single BG cell microdomain (n=4 mice per group).

Nat8l ASO therapy

An locked nucleic acid antisense oligonucleotide (“LNA-ASO”, Smith and Zain, 2019) designed by Qiagen to knockdown Nat8l expression (“Nat8l ASO”, nucleotide sequence GGCGTAGAGCAGTTGG) and a negative control LNA-ASO with no known eukaryote targets

("control ASO", nucleotide sequence AACACGTCTATACGC) were injected intracisternally into 2 month old sex-matched WT or CD Mice (0.5 nmol in 5 µL of artificial cerebrospinal fluid, rate of 1µL/min; under isoflurane anesthesia). Brain tissue was harvested for analysis at 7 days-, 14 days-, and 2 months-post treatment. For full details refer to Hull et al., 2020.

Statistics

Quantitative data are presented in the figures as means ± SEM. Statistical analyses were done by 2-tailed, unpaired student's t test (with Bonferroni correction for multiple comparisons where appropriate) or one- or two-way ANOVA with post-hoc Tukey's test as indicated in figure legend.

4.4 RESULTS

Canavan disease mice ("CD mice") homozygous for the $Aspa^{nur7}$ nonsense mutation have no detectable ASPA by Western blot assays and exhibit brain vacuolation by postnatal day 14 (p14) and ataxic gait by p21 [22]. Loss of ASPA results in marked over-accumulation of NAA in brain tissue of CD mice [25,83] and in significantly lower rotarod retention times than wildtype (WT) mice (**Figure 4.1a**). CD mice also exhibit prominent vacuolation throughout the brain by p30, apparent in cerebellar (**Figure 4.1b**, left panel) and thalamic (**Figure 4.1b**, right panel) white matter that has been immunostained for the myelin marker MBP (myelin basic protein). Widespread astrogliosis is also present in the brain in adult CD mice, visible in highly immunoreactive GFAP+ astrocytes of both the thalamus and cerebellum (**Figure 4.1b**). Quantification reveals that cerebellar and thalamic vacuolation is significantly higher in CD mice than in WT mice (**Figure 4.1c**). We do not observe sexual dimorphism in CD mice, and have reported previously that NAA levels and rotarod performance are similar in male and female CD mice [25].

There is significant disruption to the morphology of Bergmann glia (BG) of the cerebellum in CD mice, including fragmented and irregular processes that lose linearity and exhibit swelling. These changes are visualized in tissue sections from transgenic mice that express GFP under

the aldehyde dehydrogenase 1 family member L1 (Aldh1L1) promoter (Aldh1L1-eGFP mice) that have been co-immunolabelled for the BG cytoskeletal marker vimentin (**Figure 4.2a**, **4.2b**).

S100β, a cytosolic astrocyte marker, is reduced in the molecular layer of CD mice, and S100β+ BG somata lose their characteristic spherical shape (obvious in WT cerebellum), becoming irregular and asymmetrical in CD mice with many BG cell bodies being translocated out of the Purkinje cell (PC) layer (**Figure 4.2c**). Volumetric analysis (Imaris 9.7, Bitplane) reveals that CD mice have an increased Aldh1L1-eGFP volume per BG cell (**Figure 4.2d**) with a higher

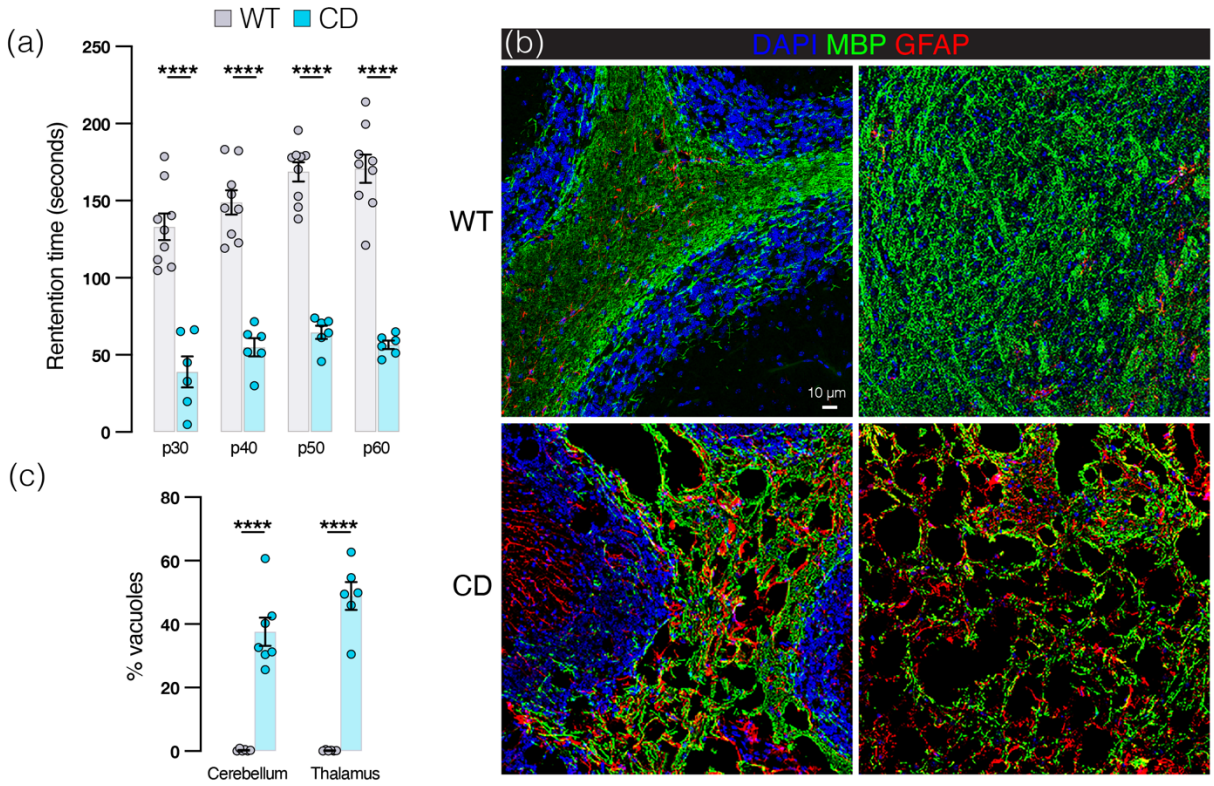

Figure 4.1: Canavan disease mice present with ataxia and widespread brain vacuolation.
(a) Rotarod retention times in seconds(s): p30: WT: 133 ± 9, CD: 39 ± 10; p40: WT: 149 ± 8, CD: 55 ± 6; at p50 WT: 169 ± 6, CD: 65 ± 4; and p60 WT: 171 ± 9, CD: 57 ± 3. $p<0.0001$ for all comparisons by 2-tailed Student's t test. $p<0.0001$ for both by two-tailed Student's t-test **(b)** Representative tissue sections from adult WT (top panel) and CD (bottom panel) mouse cerebellum (left panels) and thalamus (right panels) immunolabelled with antibodies against myelin marker MBP (myelin basic protein; green), astrocyte marker GFAP (glial fibrillary acidic protein; red) and counterstained with DAPI (blue). **(c)** Percent white matter vacuolation in adult murine cerebellum (WT: 0.3 ± 0.1%, CD: 37.7 ± 4.4%) and thalamus (WT: 0.2 ± 0.1%, CD: 48.9 ± 4.4%). Scale bar=50µm. (For all graphs: WT=gray and CD=blue. Data points represent averages for individual mice. Values reported are means (column height) ± SEMs (error bars). ****$p < 0.0001$).

variability than WT mice. CD mice also have a higher vimentin volume per cell than WT mice (**Figure 2e**). Quantification of BG process specific features demonstrates that CD mice have an increase in process volume per cell (**Figure 4.2f**) and that these processes also have a higher

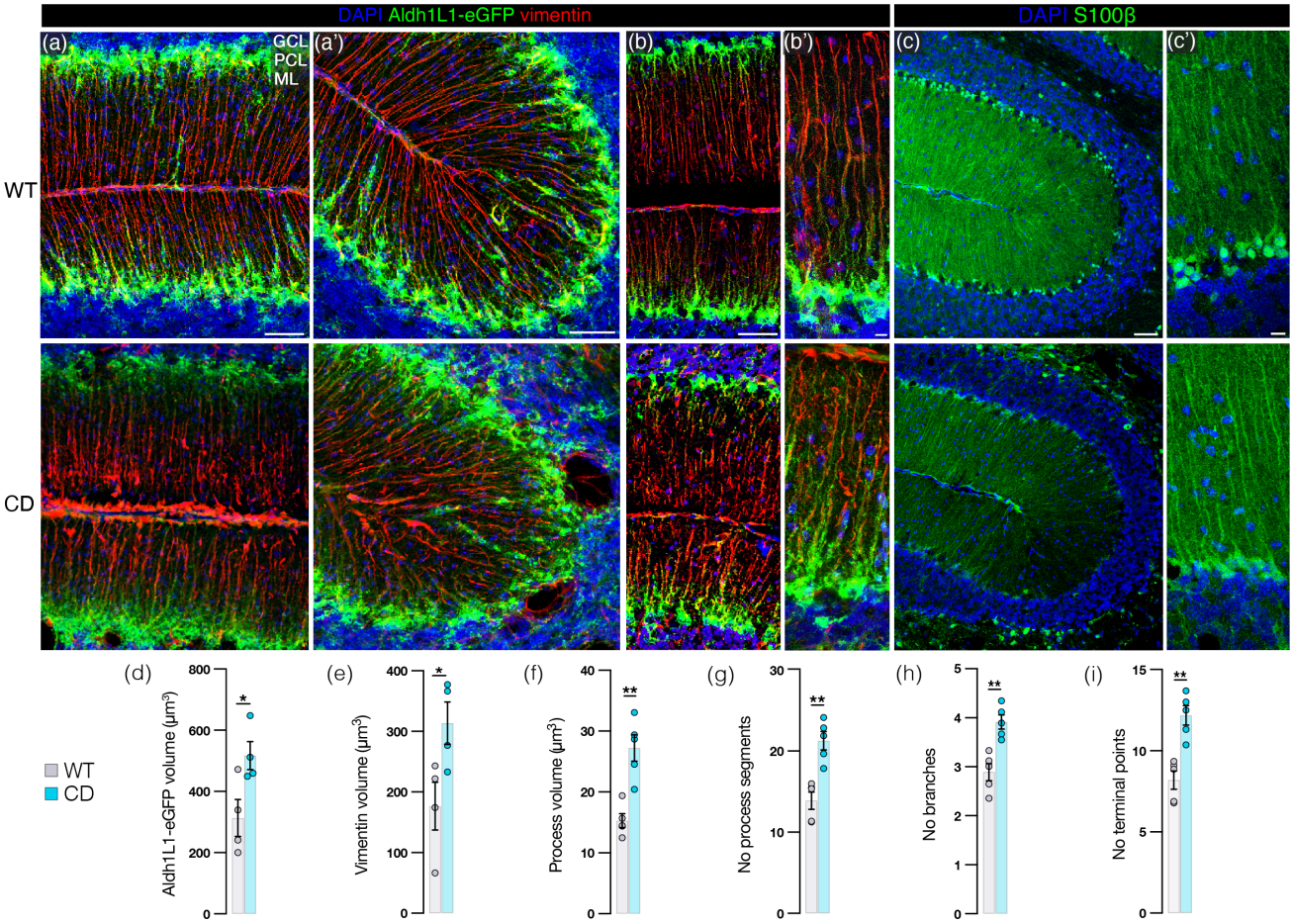

Figure 4.2: Bergman glia exhibit discontinuous, swollen processes and irregular somatic morphology and position in Canavan disease mice.
(a-b) Representative confocal images of cerebellar sections showing the granule cell layer (GCL), Purkinje cell layer (PCL) and molecular layer (ML) from p60 WT (top panel) and CD (bottom panel) transgenic Aldh1L1-eGFP mice, co-immunolabelled with BG cytoskeletal marker vimentin (red) and DAPI (blue). **(a), (a')** 30 micron z-stack images (scale bar=50 microns). **(b)** 10 micron z-stack images (scale bar=50 microns). **(b')** High power view of (b') (scale bar=10 micron). **(c)** Cerebellar sections from p60 WT (top panel) and CD (bottom panel) mice immunostained with pan-astrocyte marker S100β (green) and DAPI (blue) (scale bar=50 µm). **(c')** Higher power view of (c). (scale bar=10 µm). **(d)** Average Aldh1L1-eGFP volume (µm³) per BG cell: WT: 313.3 ± 60.6, CD: 517.2 ± 45.6. p=0.0361 by 2-tailed Student's t test. **(e)** Average vimentin volume (µm³) per BG cell: WT: 176.5 ± 39.4, CD: 313.4 ± 35.0. p=0.0408 by 2-tailed Student's t-test. **(f-i)** Quantification of BG processes specific features in molecular layer: **(f)** Process volume µm³ (WT: 15.3 ± 1.1, CD: 27.2 ± 2.1; p=0.0048), **(g)** Number of process segments: WT: 13.9±1.1, CD: 21.3±1.1; p=0.0056), **(h)** Number of process branches (WT: 2.9±0.2, CD: 3.9±0.1; p=0.0076). **(i)** Number of terminal points (WT: 8.2±0.6, CD: 12.2±0.6; p=0.0052). (f-i) p values by 2-tailed Student's t-tests with Bonferroni correction for multiple comparisons. (For all graphs: WT=gray and CD=blue. Data points represent averages for individual mice. Values reported are means (column height) ± SEMs (error bars). *p < 0.05; **p < 0.01).

number of segments (**Figure 4.2g**), branches (**Figure 4.2h**), and terminal points (**Figure 4.2i**) than in WT mice. We previously reported a substantial diminution in dendritic length and spine density in Purkinje cells (PCs) in CD mice (Hull & Wang et al. 2020). We noticed that damage to PC dendrites is also associated with major disruptions to BG cell morphology. Here, we observe that BG soma (evenly expressing SOX2 and consistently distributed in the PC layer of WT mice) are weakly SOX2+, irregularly shaped and dislocated from their natural position in CD mice (**Figure 4.3a**). Vimentin+ BG processes are enlarged, fractured and/or absent in large swaths

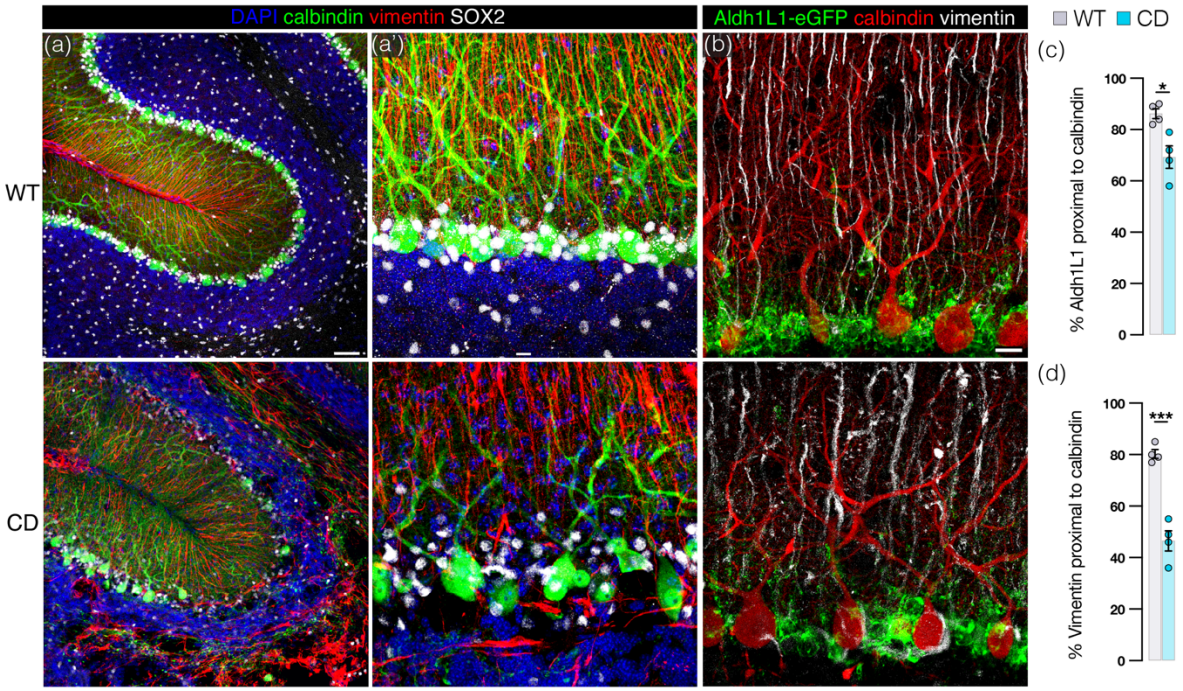

Figure 4.3: Bergmann glia-Purkinje cell interactions are disrupted in Canavan disease mice.
(a) Representative confocal images (30 micron z-stack) of cerebellar sections from adult WT (top panel) and CD (bottom panel) mice immunolabelled with Purkinje cell (PC) marker calbindin (green) and BG markers vimentin (cytoskeletal, red), SOX2 (somatic, white) counterstained with DAPI (blue) (scale bar=50 µm). High power view shown in **(a')** (scale bar=10 µm). **(b)** 4 micron z-stack confocal images from Aldh1L1-eGFP+ (green) WT (top panel) and CD (bottom panel) mice co-stained with calbindin (red) and vimentin (white) (scale bar=10 µm). **(c)** Percent of BG marker Aldh1L1-eGFP within 1 micron proximity of PC marker calbindin in CD (69.25 ± 4.4) and WT (86.2 ± 1.9) mice (p=0.0121 by two-tailed Student's t test). **(d)** Percent of BG process marker vimentin within 1 micron proximity of PC marker calbindin in CD (46.5 ± 4.0) and WT (80.3 ± 1.7) mice (p=0.0002 by two-tailed student's t test). (For all graphs: WT=gray and CD=blue. Data points represent averages for individual mice. Values reported are means (column height) ± SEMs (error bars). *$p < 0.05$, ***$p < 0.001$).

from areas where calbindin+ PC dendrites are simplified and/or missing in CD mice (**Figure 4.3a, 4.3b**).

These features are in marked contrast to WT BG processes, which exhibit a more consistent diameter and even spacing throughout the molecular layer where they are intricately interwoven with complex PC dendritic arborization (**Figure 4.3a, 4.3b**). Aldh1L1-eGFP signal from BG cell bodies in the PC layer of CD mice is irregular with hypo- and hyper-intense regions, compared to the consistent signal present in WT mice (**Figure 4.3b**). We generated 3D reconstructions of confocal images in Imaris which allowed for proximity analysis between Aldh1L1-eGFP+/vimentin+ BG and calbindin+ PCs. The results reveal that a lower percentage of Aldh1L1-eGFP and vimentin signal, respectively, are within 1 micron of PC marker calbindin in CD mice (**Figure 4.3c, 4.3d**). Taken together, these data demonstrate a significant reduction in BG-PC interactions in the CD cerebellum.

We reasoned that a reduction in the number of interactions between BG and PC dendrites could result in the loss of synaptic contacts between the parallel fibers (PFs) of the excitatory granule cells (GCs) and PC dendrites, synapses which are typically enwrapped and supported by BG microdomains. Coinciding with irregular BG and PC morphology in CD mice (**Figure 4.4a**, top and bottom panels), immunostaining for vesicular glutamate transporter 1 (VGLUT1)+ PF-PC synapses reveals a marked reduction of signal in CD mice (**Figure 4.4b, 4.4b'**) as compared to WT mice (**Figure 4.4a, 4.4a'**), quantified by mean fluorescence intensity (MFI, Figure 4c).There is a visible decrease in VGLUT2+ CF terminals in the molecular layer of CD mice (**Figure 4.4e, 4.4e', 4.4f, 4.4f'**), which we quantified in Imaris by counting the number of VGLUT2+ puncta in the molecular layer (**Figure 4d**). VGLUT2 signal also appears more concentrated around PC soma in CD mice than WT mice (**Figure 4.4e', 4.4f'**)

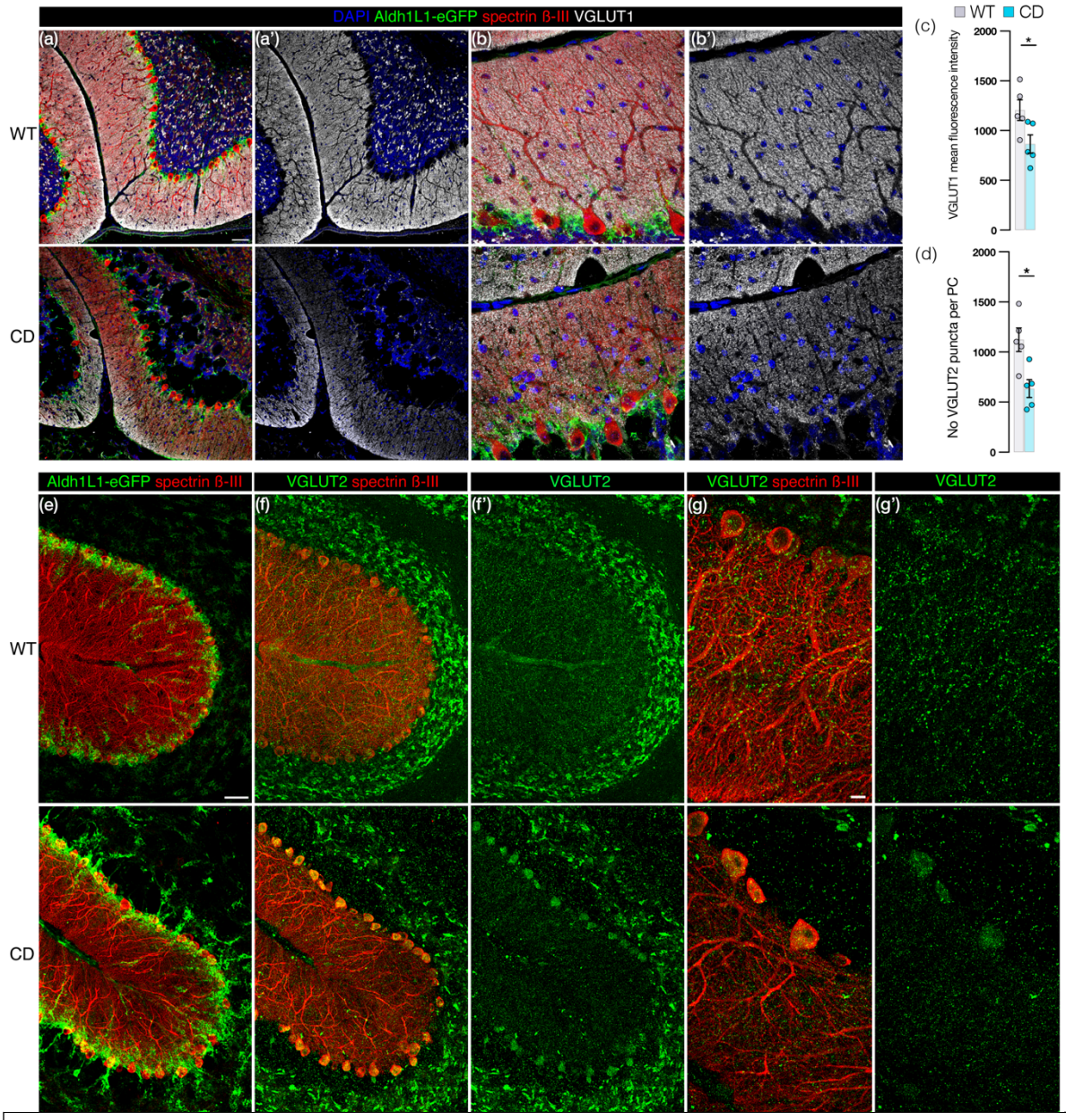

Figure 4.4: Loss of parallel fiber- and climbing fiber-Purkinje cell synapses in Canavan disease mice.

(a) Representative images from adult WT (top panel) and CD (bottom panel) Aldh1L1-eGFP+ (green) mice immunostained with PC marker Spectrin β-III (red), PF-PC synaptic marker VGLUT1 (white) and DAPI (blue) with VGLUT1 and DAPI in isolation in (a') (scale bar=50 μm). **(b)** High power images of (a), VGLUT1 and DAPI isolated in (b') (scale bar=10 μm). **(c)** Mean fluorescence intensity of VGLUT1 signal in the molecular layer in CD (865 ± 92, blue) and WT (1206 ±104) mice ($p=0.0397$ by two-tailed student's t test). **(d)** Average number of VGLUT2+ puncta per PC in CD (635 ± 89) and WT (1123 ± 117) mice ($p=0.0106$ by two-tailed student's t test). **(e-f)** Low power images (scale bar: 50 μm) from Aldh1L1-eGFP+ WT (top panel) and CD (bottom panel) mice: **(e)** Aldh1L1-eGFP (green) and spectrin β-III (red). (f) CF-PC synapse marker VGLUT2 (green) and spectrin β-III (red). **(f')** VGLUT2 (green) signal isolated. **(g)** High power view (scale bar=10 μm) of (f), VGLUT2 (green) and spectrin β-III (red). **(g')** VGLUT2 (green) signal isolated. (For all graphs: WT=gray and CD=blue. Data points represents averages for individual mice. Values reported are means (column height) ± SEMs (error bars). *$p < 0.05$; **$p < 0.01$).

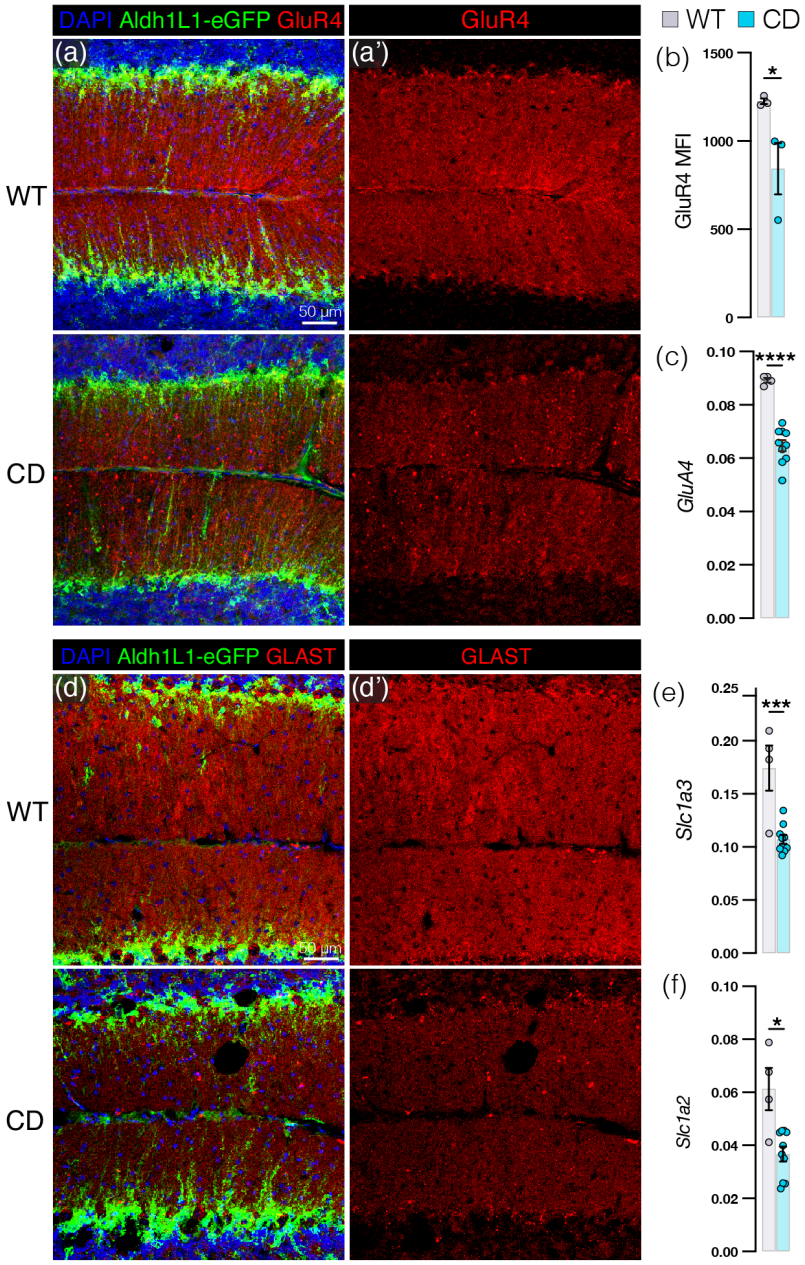

Figure 4.5: Bergmann glia exhibit a loss of Ca2+-permeable ampars and glutamate transporters in Canavan disease mice.
(a) Representative cerebellar sections from adult WT (top panel) and CD (lower panel) Aldh1L1-eGFP+ (green) mice immunostained for Ca^{2+}-permeable AMPAR subunit GluR4 (red) and counterstained with DAPI (blue) with GluR4 signal isolated in **(a')** (scale bar=50 μm). **(b)** Mean fluorescence intensity of GluR4 in molecular layer of WT (1225 ± 16) and CD (843 ± 145) mice (p=0.047 by one-way ANOVA, full comparisons shown in Figure 8b). **(c)** Relative *GluA4* mRNA abundance (normalized to *Hsp90*) by qRT-PCR in WT (0.089 ± 0.00087) and CD (0.064 ± 0.0021) mice (p<0.0001 by one-way ANOVA, full comparisons shown in Figure 8c). **(d)** Representative cerebellar sections from WT (top panel) and CD (lower panel) Aldh1L1-eGFP+ (green) mice immunostained for glutamate transporter GLAST (red) and counterstained with DAPI (blue), with GLAST signal isolated in (d') (scale bar=50 μm). **(e)** Relative *Slc1a3* (encodes GLAST) mRNA abundance (normalized to *Hsp90*) by qRT-PCR in WT (0.17 ± 0.021) and CD (0.11 ± 0.013) mice (p=0.0003 by one-way ANOVA with post hoc Tukey's test, full comparisons shown in Figure 8e). **(f)** Relative *Slc1a2* (encodes GLT-1) mRNA abundance (normalized to Hsp90) by qRT-PCR in WT (0.061 ± 0.0080) and CD (0.37 ± 0.0028) mice (p=0.0221 by one-way ANOVA, full comparisons shown in Figure 8f). (For all graphs: WT=gray and CD=blue. Data points represent individual mice. *p < 0.05; ***p < 0.001; ****p < 0.0001).

Given the loss of BG-PC proximity and PF-PC/CF-PC synapses in the molecular layer, we decided to explore other features of BG microdomains that could also be disrupted in CD. BG microdomains highly express AMPARs with a particular subunit composition (expression of GluR1 and GluR4 subunits, encoded by *GluA1* and *GluA4*

respectively and absence of GluR2, encoded by *GluA2*) that confers calcium permeability in the presence of glutamate (Burnashev et al., 1992, Müller et al., 1992, Keinänen et al., 1990). GluR4 is unique to BG AMPARs in the molecular layer, and indeed CD mice exhibit a visible decrease in GluR4 protein level by immunohistochemistry (**Figure 4.5a**) and GluR4 mean fluorescence intensity (**Figure 4.5B**) in the molecular layer. *GluA4* message level in whole cerebellar tissue of CD mice is lower than in WT (**Figure 4.5b**). BG processes also abundantly express glutamate transporters GLAST and, to a lesser extent, GLT-1, which have demonstrated roles in glutamate reuptake (Bergles et al., 1997). We find that CD mice exhibit a decrease in GLAST protein level visible by

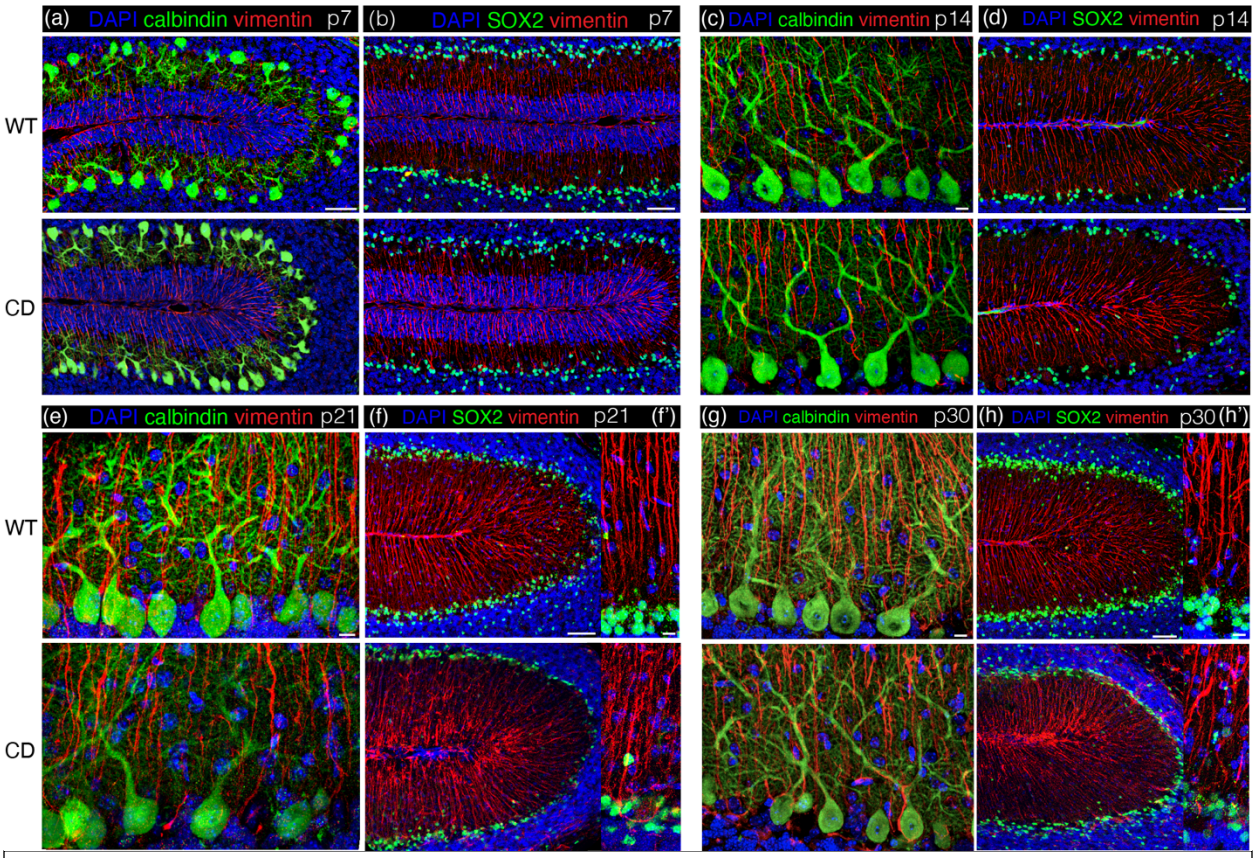

Figure 4.6: Bergmann glia and Purkinje cell alterations appear between p14 and p21 in Canavan disease mice.
Representative cerebellar sections from WT (top panel) and CD (bottom panel) mice at p7 (a, b), p14 (c, d), p21 (e, f, f') and p30 (g,g',h,h'). Sections displayed in a, c, e, and g are stained with DAPI (blue), PC marker calbindin (green), and BG process marker vimentin (red). Sections displayed in b, d, f, and h are stained with DAPI (blue), BG somatic marker SOX2 (green) and BG process marker vimentin (red). Scale bar=50 µm for a, b, d, f, h and 10 µm for c, e, f', g, and h'.

IHC (**Figure 5d**) in the molecular layer as well as a decrease in total cerebellar *Slc1a3* (encodes GLAST**, Figure 5e**) and *Slc1a2* (encodes GLT-1, **Figure 5f**) mRNA. In sum, we find that BG in CD mice demonstrate significant losses to synapse-supporting microdomain proteins.

Next, we sought to determine the age at which cerebellar cellular abnormalities first arise in CD mice. At p7, immature PCs (**Figure 4.6a**) and BG (**Figure 4.6a, 4.6b**) appear similar in WT and CD mice but by p14, a slight increase in vimentin immunoreactivity becomes observable in BG processes of CD mice (**Figure 4.6c, 4.6d**).

By p21, BG irregularities and PC dendritic abnormalities are clearly visible in CD mice (**Figure 4.6e, 4.6f, 4.6f'**), worsening by p30 (**Figure 4.6g, 4.6h, 4.6h'**). Processes in p21 CD mice are swollen, particularly in distal regions, and exhibit irregular lateral protuberances, while somas also begin to take on the asymmetrical shape seen in adult CD mice (**Figure 4.6e, 4.6f. 4.6f', 4.6g, 4.6g'**). PCs in CD mice at p21 (**Figure 4.6e**) and p30 (**Figure 4.6g**) exhibit less complex dendritic branching and show a less continuous relationship with BG processes, consistent with our findings in more mature mice (**Figure 4.3**). These observations suggest that the critical window for BG-PC degeneration occurs between p14 and p21.

To better understand the functional implications of altered BG morphology we performed imaging using the calcium indicator Fluo4-AM in acute cerebellar slice preparations from mice aged p21-p30 when, as we have established, BG alterations are already present. In addition to broad full-cell and multi-cell spanning calcium waves, we observed spontaneously occurring compartmentalized/localized calcium transients in BG processes (marked by the astrocyte specific dye SR101[84,85]) that were ~1-2 microns wide (**Figure 4.7a**, with representative traces from CD and WT mice in **Figure 4.7b**). These transients are consistent with signals observed in BG during *in vivo* calcium imaging in awake behaving mice [85] and acute slice preparations [65]. Quantification of these calcium transients reveals that CD mice have a significantly lower frequency of spontaneous events than WT mice (**Figure 4.7c**). The duration of these events is

also significantly prolonged in CD mice (**Figure 4.7d**), while the rise time remains similar to WT mice (**Figure 4.7e**). Stimulation of slices with AMPA increases the frequency of localized transients in CD and WT mice (data not shown) but does not affect transient duration or rise time (**Figure 4.7c, 4.7d**). Overall, we find that BG in CD mice exhibit less spontaneous calcium activity and the duration of spontaneous or AMPA-evoked single events is prolonged with no change in rise time.

We previously developed an antisense oligonucleotide (ASO) targeting the knockdown of the NAA-synthesizing enzyme NAT8L ("Nat8l ASO") with the prediction that decreasing elevated levels of brain NAA would be therapeutic for CD mice. Intracisternal delivery of this Nat8l ASO to adult, symptomatic CD mice reversed spongiform vacuolation and ataxia within two weeks of

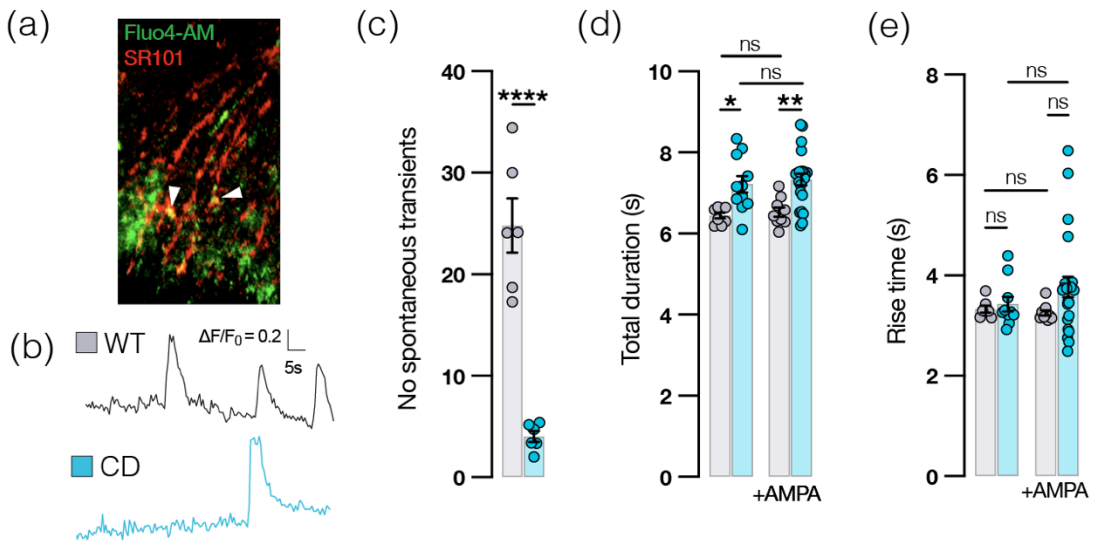

Figure 4.7: Bergmann glia Ca^{2+} transients are less frequent and prolonged in Canavan disease mice.
(a) Representative view of Fluo4-AM Ca^{2+} transients (green) co-localized with astrocyte-specific SR101 dye (red) in BG processes (arrowheads) in an acute cerebellar slice **(b)** Representative BG Ca^{2+} traces from WT and CD mice. **(c)** Frequency of spontaneous transients in BG per minute in 1000 μm^3 ROI. Each data point represents the average of 3 ROIs for 1 mouse (WT: 25.0 ± 2.7, CD: 4.0 ± 0.54; p= <0.0001 by two-tailed student's t test). **(d)** Total duration (s) of spontaneous (WT: 6.5 ± 0.074, CD: 7.2 ± 0.21; p= 0.0321) and AMPA-evoked (WT: 6.5 ± 0.12, CD: 7.3 ± 0.15; p=0.0064) transients (comparisons by one-way ANOVA with post hoc Tukey's test). **(e)** Rise time of spontaneous (WT:3.3 ± 0.070, CD: 3.4 ± 0.15, ns) and AMPA-evoked transients (WT: 3.3 ± 0.055, CD: 3.8 ± 0.21, ns) (all comparisons by one-way ANOVA with post hoc Tukey's test). For (d-e) each data point represents the average of one microdomain over a 5-min recording window from n=4 mice per group. (For all graphs: WT=gray and CD=blue. Values reported are means (column height) ± SEMs (error bars). *p < 0.05; **p

treatment and repaired PC dendritic atrophy leading to an increase in PC spine density[25]. We wondered if BG damage was also reversible with this treatment and indeed, BG in Nat8l ASO treated mice demonstrate more intact morphology than untreated controls (**Figure 4.8a**). Treatment also results in an increase in GluR4 immunostaining (**Figure 4.8b**) and GluR4 mean fluorescence intensity (**Figure 4.8c**) in the molecular layer of Nat8l ASO treated CD mice (30 days post treatment) when compared to untreated CD mice or CD mice treated with a control ASO with no known eukaryotic targets ("Ctrl-ASO"). These data correspond with an increase in *GluA4* message level which climbs to WT levels by 60 days post-administration (**Figure 4.8d**). Message levels of *Slc1a3* (**Figure 4.8e**) and *Slc1a2* (**Figure 4.8f**) all increase over time in Nat8l ASO treated CD mice, ultimately also reaching WT levels. In summary, we find that Nat8l ASO therapy improves BG morphology and increases BG microdomain protein expression in CD mice.

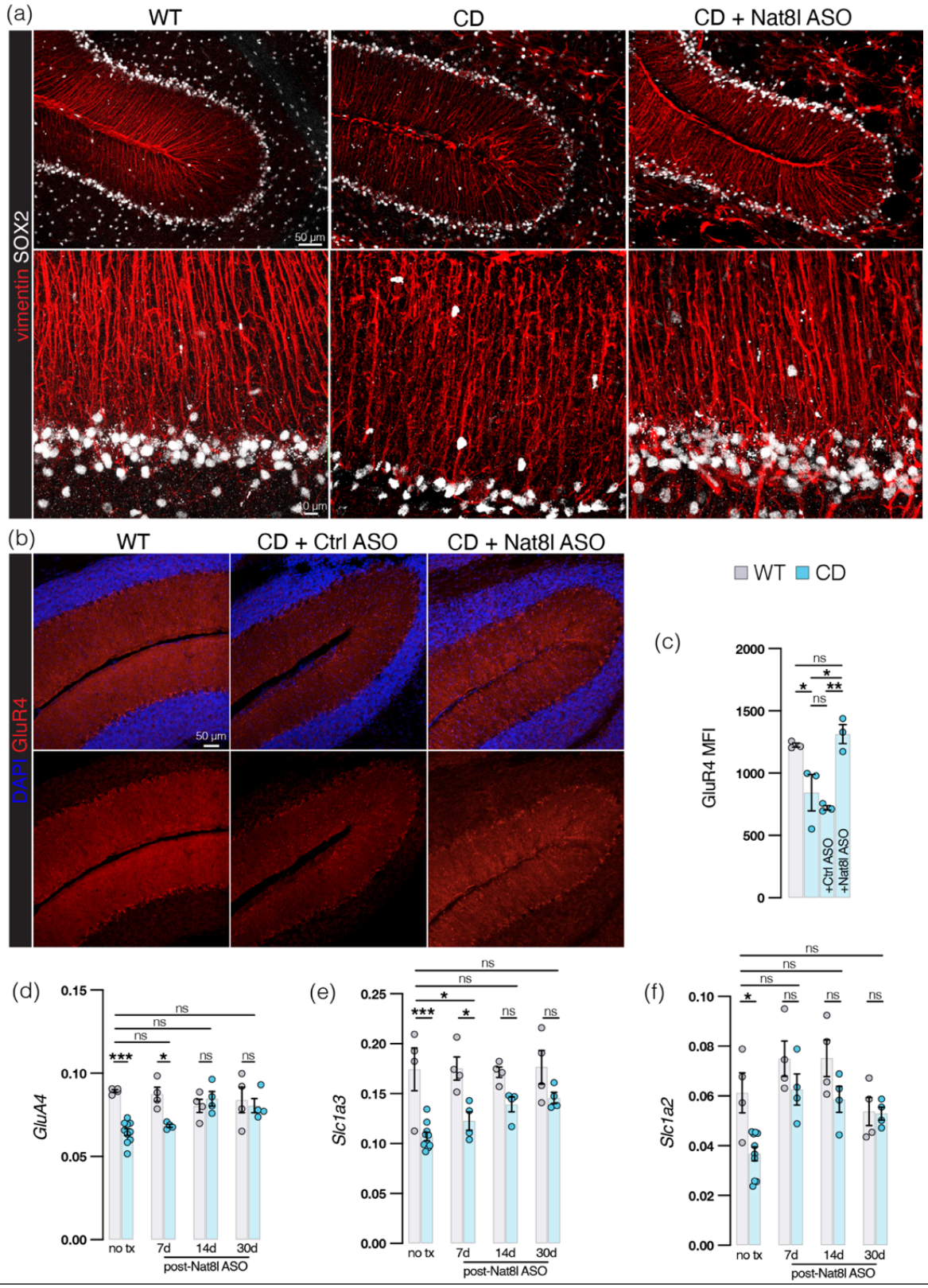

Figure 4.8: Antisense oligonucleotide therapy repairs Bergmann glia irregularities observed in Canavan disease mice. *(Legend continues on next page)*

Figure 4.8: Antisense oligonucleotide therapy repairs Bergmann glia irregularities observed in Canavan disease mice.
(a) Representative cerebellar sections immunostained with BG process marker vimentin (red) and BG somatic marker SOX2 (white) from WT (left), CD (middle) and CD mice 60 days after intracisternal injection of Nat8l ASO (right) at low (top panel, scale bar = 50 µm) and high (bottom panel, scale bar = 10 µm) power. **(b)** Representative cerebellar sections immunostained with marker for Ca^{2+}-permeable AMPAR subunit GluR4 (red) and DAPI (blue) from WT BG process marker vimentin (red) and BG somatic marker SOX2 (white) from WT, CD and Nat8l ASO treated CD mice, 60 days post treatment at low (top panel, scale bar = 50 µm) and high (bottom panel, scale bar = 10 µm) power. **(c)** Mean fluorescence intensity of GluR4 in molecular layer of untreated WT (1225 ± 16) and CD (843 ± 145) (same data shown in Figure 5b) mice as well as CD mice treated with control (ctrl) ASO (721 ± 18) and CD mice treated with Nat8l ASO (1314 ± 76) 60 days post-administration. p values by one-way ANOVA with post hoc Tukey's test: WT vs. CD: p=0.0479, CD + Nat8l ASO vs CD: p=0.0167, CD + Nat8l ASO vs CD + Ctrl ASO: p=0.0044. **(d)** Relative *GluA4* mRNA abundance (normalized to *Hsp90*) by qRT-PCR in untreated WT (0.089 ± 0.00087) and CD (0.064 ± 0.0021) mice (p<0.0001, same data shown in Figure 5c) and Nat8l ASO treated mice 7d-post (WT:0.087 ± 0.0042, CD:, 0.068 ± 0.00096, p=0.0443), 14d-post (WT: 0.080 ± 0.0040, CD:0.085 ± 0.0044, ns), and 60d-post (WT:0.084 ± 0.0076, CD: 0.081 ± 0.0043, ns) injection (comparisons by one-way ANOVA with post hoc Tukey's test). **(e)** Relative *Slc1a3* mRNA abundance (normalized to *Hsp90*) by qRT-PCR in untreated WT (0.17 ± 0.021) and CD (0.11 ± 0.013, blue) mice (same data presented in Figure 5e, p=0.0003), 7 days post treatment with Nat8l ASO in WT (0.18 ± 0.0041) and CD (0.12 ± 0.018) mice (p= 0.0352), 14 days post treatment with Nat8l ASO in WT (0.17 ± 0.011) and CD (0.14 ± 0.015) mice (ns) and 30-days post treatment with Nat8l ASO in WT and CD mice in WT (0.18 ± 0.0041) and CD (0.15 ± 0.011) mice (ns) (comparisons by one-way ANOVA with post hoc Tukey's test). **(f)** Relative *Slc1a2* mRNA abundance (normalized to *Hsp90*) by qRT-PCR in WT (0.061 ± 0.0080) and CD (0.37 ± 0.0028) mice (same data presented in Figure 5f, p=0.0221), 7 days post treatment with Nat8l ASO in WT (0.075 ± 0.0071) and CD (0.063 ± 0.0062) mice (ns), 14 days post treatment with Nat8l ASO in WT (0.075 ± 0.0073) and CD (0.059 ± 0.0052) mice (ns) and 30-days post treatment with Nat8l ASO in WT and CD mice in WT (0.054 ± 0.0056) and CD (0.053 ± 0.0026) mice (ns) (comparisons by one-way ANOVA with post hoc Tukey's test). (For all graphs: WT=gray and CD=blue, treatments specified. Values reported are means (column height) ± SEMs (error bars). *p < 0.05; **p < 0.01; ***p < 0.001).

4.5 DISCUSSION

The hallmark of CD is elevated brain NAA which, by an unknown mechanism, results in widespread astroglial dysfunction, demonstrated here in BG of CD mice (see our prior work Wang *et al.*, 2021 for a discussion on how NAA overloading in astrocytes could be a primary driver of CD pathogenesis). The compromised structural integrity of BG and retraction of BG processes from PC dendrites may be the underlying cause of PC simplification in CD mice. Unsurprisingly, a reduction in BG-PC overlap coincides with a decrease in PF-/CF-PC synaptic inputs in CD mice, likely resulting from impaired synaptic support. PFs influence simple spike firing in PCs and have important roles in locomotion, motor coordination and motor learning [86–88] while CF input drives

complex spikes, helping with movement adjustment and fine motor coordination . CF and PF inputs to PCs are also critical for motor learning and adaptation [89,90].

We show that by p21, but not before p14, CD mice exhibit irregularities in both BG and PC, coinciding with the first signs of motor disturbances [22]. Further investigation could uncover if BG dysfunction predates PC alterations in the intervening period (p15-p20). BG differentiation is temporally and functionally correlated with PC dendritic outgrowth and synaptogenesis in the molecular layer [91]. Disruption to PF synaptogenesis, ongoing until p25, could cause the loss of PF-PC synapses we observe in adult CD mice. PF-PC synaptic dysfunction is common in multiple mouse models of spinocerebellar ataxia (SCA) [92], many of which also present with BG dysfunction [93–95]. CF-PC synapse formation occurs in several stages, where early on, multiple CF inputs are selectively pruned so that by p19, only one CF innervates each PC [96,97]. Proper CF-PC innervation is critically dependent upon the concurrent, undisturbed progression of PF-PC synaptogenesis [98]. Damage to BG and PCs coupled with alterations to PF-PC synaptic development may interrupt the normal CF pruning process, resulting in persistent multiple CF-PC innervation. PF-PC synaptic dysfunction is also common in several mouse models of ataxia (including the ATXN1 mouse) and frequently observed in conjunction with multiple CF innervation [99–103]. Disruption of CF-PC synapses is also seen in postmortem tissue from patients with spinocerebellar ataxias, Parkinson's disease, and essential tremor [92,104,105].

In addition to facilitating glutamate reuptake and shaping the time course of post-synaptic receptor activation [69,106,107], GLAST and GLT-1 also protect against extrasynaptic glutamate spillover [108,109] and prevent prolonged glutamate elevation which can contribute to excitotoxicity [110]. GLAST and GLT-1 have also been shown to decrease the activation of AMPARs on PCs at PF-PC synapses during repeated stimulation [111]. GLAST-null mice are unable to appropriately prune multiple CF-PC innervation during development, resulting in alterations to CF-evoked excitatory postsynaptic currents (EPSCs) in addition to disturbances in PF-PC synapses [112],

neuronal atrophy [113], and motor discoordination [114], all features we have now documented in CD mice. Combined deletion of GFAP and GLAST in BGs also impairs PC synaptogenesis and furthermore initiates LTD [114,115]. GLAST loss is seen in multiple spinocerebellar ataxias [116,117], Alzheimer's disease [118], and more specifically, BG GLAST depletion in ATXN1 mice has been associated with PC loss [119]. PCs do, in fact, express the glutamate transporter EAAT4 which participates in reuptake but to a much lesser extent than glial glutamate transporters [120].

In addition to glutamate transporters, BG microdomains also feature Ca^{2+}-permeable AMPARs that possess a relatively high Ca^{2+} conductance even in low calcium [72] which results in a robust reduction in the resting BG potassium conductance [121]. Loss of GluR4 (and *GluA4* transcript) indicates that Ca^{2+}-permeable AMPARs are reduced in BG of CD mice which could explain why BG processes retract from PC dendrites, given that influx of Ca^{2+} through these AMPARs is considered the primary mechanism by which BG can "sense" functional synapses when they first become active [34,122]. Ca^{2+}-permeable AMPARs have also been shown, in cultured BG cells, to regulate the expression of GLAST [123]. Loss of BG-specific Ca^{2+}-permeable AMPARs results in BG process retraction from PC synapses (consistent with our findings in CD mice), increases in the amplitude and duration of PC currents, delays in glutamatergic synapse formation and disturbances in fine motor coordination in developing mice [73]. Disrupting Ca^{2+} permeability in BG AMPARs also results in retraction of BG processes from PC synapses, significantly prolonging EPSCs in PCs resulting from PF or CF stimulation and leading to multiple innervation of PCs by CFs [122]. Conversely, overexpression of BG AMPARs drives the extension and overgrowth of BG processes [124]. BG AMPARs are therefore not only crucial for regulating the structural and functional establishment of microdomains during development but are also integral to synaptic stability and axonal outgrowth in adults. Retraction of BG processes from PCs may be the result of decreased Ca^{2+} influx due to AMPAR loss, resulting in multifaceted dysfunction in CD mice.

We also observed a loss of spontaneous calcium activity and an increase in the total duration, but not the rise time, of BG spontaneous and AMPA-stimulated localized calcium transients in CD mice. These signals are consistent with “calcium sparkles” reported by Nimmerjahn et al. (2009) to occur in BG during *in vivo* calcium imaging of awake, behaving animals purportedly as the result of either synaptic activity or intracellular calcium waves occurring within the fine processes of BG. The Ca^{2+} transients we recorded are also consistent with spontaneous and PF-stimulation induced signals isolated to BG microdomains in cerebellar slices [65]. When visualized by EM, microdomains show complete BG ensheathment of PC synapses, providing evidence that these signals are of synaptic origin [65]. Prolonged synaptic presence of glutamate due to reduced GLAST expression seen in CD mice could prolong glutamate receptor activation in BGs and increase calcium transient duration, thus compromising intracellular calcium buffering. The implications of a loss of spontaneous BG activity and prolonged intracellular calcium elevation are widespread (see Shigetomi, Patel and Khakh, 2016 for a review of calcium signaling in astrocytes)[125]. Using optogenetic stimulation, Sasaki et al. (2012) showed that increased intracellular calcium in BG induces glutamate release, activates AMPARs on PCs, induces LTD in PF-PC synapses, and ultimately leads to disturbances in associative motor learning and/or motor performance of cerebellar mediated behaviors.[126] K^+ uptake by BGs is a Ca^{2+}-dependent processes known to regulate PC membrane potential. Indeed, PCs show an increase in spike activity when extracellular K^+ is depleted due to increased BG Ca^{2+} signaling in acute slices and *in vivo* [71]. Activation of BG AMPARs also strongly inhibits BG-BG gap junctional coupling [127] and increased intracellular calcium in astrocytes has been shown to elevate intracellular calcium in neighboring neurons [128,129].

The integral roles that BG play in cerebellar structural and functional development are highly evident given the strong phenotypes associated with BG dysregulation and damage, many of which have been demonstrated here in CD mice. BG actively participate in cerebellar

information processing by regulating synaptogenesis and supporting synaptic activity, indirectly via ion buffering and careful shaping of the glutamate curve, and/or directly via calcium signaling, glutamate release, and upstream activation of LTD pathways at PF-PC synapses [66]. Our results indicate disruptions to all of these functions in CD mice. Given the intimate relationship between BG and PCs, and PC strong reliance on BG for synaptic development, stability and ongoing support, BG damage may well be a non-cell autonomous mechanism of PC degeneration in the cerebellar ataxias. We are encouraged by our findings that many of the alterations seen in CD mice, including BG morphological changes, loss of GluR4, and decreases in *GluA4*, *Slc1a3* and *Slc1a2* message levels, are improved by treatment with our Nat8l ASO therapy. Overall, our findings point to early disruptions to BG integrity and dysregulation of the BG-PC relationship as a driver for CD pathogenesis and warrant further investigation into potential therapeutic targets for BG repair in CD and other neurological diseases.

Table 4.1: Antibodies and Primers

Antibody	RRID		Concentration used
calbindin	AB_868617		IHC 1:200
GFAP	gift of Dr. Virginia Lee, University of Pennsylvania		IHC 1:50
GFP	AB_11181883		IHC 1:200
GLAST	AB_2811303		IHC 1:200
GluR4	AB_90711		IHC 1:300
MBP	AB_10655672		IHC 1:50
SOX2	AB_10710406		IHC 1:20
Spectrin β-III	AB_2194518		IHC 1:200
VGLUT1	AB_262185		IHC 1:200
VGLUT2	AB_1587626		IHC 1:200
vimentin	AB_10003206		IHC 1:1000
Gene name	Forward primer sequence	Reverse primer sequence	Source
Slc1a2	CAACGGAGGATATCAGTCTGC	TGTTGGGAGTCAATGGTGTC	Integrated DNA Technologies
Slc1a3	CAAGACACTGACACGCAAGGAC	CTTAACATCTTCCTTGGTGAGGC	
GluA4	GGGAGGTGACTCCAAGGACA	CCAGTGATGGATAACCTGGCT	
Hsp90	AAACAAGGAGATTTTCCTCCGC	CCGTCAGGCTCTCATATCGAAT	

CHAPTER 5 – CONCLUSIONS

5.1 SUMMARY

Taken together, the results of this work demonstrate that reducing brain NAA levels is therapeutic for CD mice. Reduction of NAA levels can both prevent and reverse CD and its symptoms, including brain vacuolation, ataxia, astroglial swelling, Bergmann glial structural abnormalities and Purkinje cell dendritic atrophy. Lowering NAA levels was achieved either by blocking the synthesis of NAA with our Nat8l ASO or by abrogating cellular uptake of NAA by ablating the plasma membrane transporter NaDC3.

5.2 NAA AS A MARKER OF NEURONAL HEALTH

Despite being the second most abundant brain metabolite next to glutamate[53], NAA remains an enigmatic molecule. Our rodent NAT8L knockout studies[21] as well as the single reported case of a patient with hypoacetylaspartia[23] demonstrate that NAA is not required for myelin synthesis as was previously postulated. NAA does, however, still provide a readily available source of acetate that is incorporated into oligodendroglial myelin.[20] NAA may also have important osmoregulatory functions in neurons, servings as a mechanism for the excretion of abundant water generated during glucose synthesis, as NAA exits in a shell of 10-12 water molecules.

Nevertheless, NAA continues to serve as an important clinical marker in neurodegenerative diseases. Decreased NAA levels, as measured by magnetic resonance spectroscopy (MRS), have traditionally been interpreted as signaling compromised neuronal metabolism or even neuronal loss.[53] NAA concentration is considered a proxy for the number of healthy neurons because it synthesized by *Nat8l* in neuronal mitochondria as a byproduct of glucose metabolism. NAA is normally found at around 20 mM in the neuronal compartment[11] and indeed, decreased NAA levels are seen in Alzheimer's disease[130], Huntington's disease[131],

Parkinson's disease[132], amyotrophic lateral sclerosis[133], multiple sclerosis[134], traumatic brain injury (TBI)[135], stroke[136], and epilepsy[137]. In MS, secondary progressive patients have lower NAA concentrations than those with the relapsing-remitting form of MS, indicating a relationship between NAA concentration and disease severity.[134] This relationship is also consistent with observations in other neurodegenerative diseases like Alzheimer's and Parkinson's.[138] In TBI, NAA levels decrease in proportion to the volume of damaged tissue.[135]

5.3 NAA NEUROTOXICITY

While neuronal loss and trauma are associated with decreased NAA, we have yet to unravel the nature of neurotoxicity when brain NAA is markedly elevated. A longitudinal proton magnetic resonance spectroscopy (H-MRS) study conducted in 28 CD patients and age-matched controls demonstrates that NAA increases linearly as CD patients age[12]. Interestingly, this H-MRS data also shows that NAA has a fronto-occipital gradient, wherein the areas with the highest NAA concentration correlate with areas of disrupted brain functionality and the most severe spongiform degeneration in CD. While this would seemingly indicate a positive correlation between cellular pathology and localized NAA concentration, results from other *in vitro* and *in vivo* rodent studies have muddied the waters.

Over-expression of the NAA-synthesizing enzyme NAT8L does not produce Canavan disease-like features and, in fact, myelination, motor function, lifespan and brain morphology all appear normal. [139] Therefore, elevated NAA appears only significantly problematic in a system with compromised ASPA functionality. Bath application of a hydrophobic methyl ester of NAA (m-NAA) does not affect cell survivability or membrane excitability in primary rodent neuronal or oligodendroglial cell cultures or in acute rodent slice preparations.[140,141] Similarly, elevating NAA to Canavan disease levels in wildtype rodents by oral administration of m-NAA did not induce any myelin or motor pathologies.[139] Utilization of m-NAA presents concerns for the interpretation of

these results, as it induces the non-physiologically relevant uptake of NAA into non-NaDC3 expressing cell types. When cells lack the ability to take up NAA via NaDC3, NAA levels remain normal in CD mice and brain vacuolation and ataxia do not develop.[36]

5.4 NAA-G

Neurotoxicity in Canavan disease could also be mediated by elevated N-acetyl-aspartyl-glutamate (NAA-G). Interestingly, NAA-G, a dipeptide derivative of NAA, is the most concentrated neuropeptide in the brain and is functionally and metabolically linked to NAA.[142] NAA levels, when measured by H-MRS or other chromatographic methods, typically reflect total NAA which is a mixture of both NAA and NAA-G. NAA-G has been shown to activate NMDA receptors *in vivo*[143] and in *in vitro* slice experiments[141] and can activate type 3 metabotropic glutamate receptors (mGluR3).[142,144] In astrocytes, this mGluR3 activation this has been linked to the downstream initiation of the astrocyte-vascular system producing focal hyperemia which directly modulates metabolite availability and energy supply to neurons.[145] Furthermore, activation of neuronal mGluR3s results in decreased voltage dependent calcium conductance, alterations in long term potentiation and depression, and inhibited GABA release.[142]

NAA-G functions as a glutamate reservoir and blocking NAA-G hydrolysis suppresses glutamate release which has been shown beneficial in many neurological disorders where NAA-G is elevated.[146–148] Similar findings have recently been reported in cancer, where both NAA-G and its catabolic enzyme that derives glutamate are found in higher levels.[149] Suppressing NAA-G hydrolysis could be beneficial strategy in Canavan disease. Further investigation into how potential disruptions in the NAA and NAA-G pathway might contribute to the pathogenesis of Canavan disease and other neurodegenerative conditions is needed.

5.5 *Slc13a3*/NaDC3 IN CANAVAN DISEASE

In Chapter 3, I described *Slc13a3* constitutive knockout as preventative for disease development in CD mice. However, we cannot divorce these findings from the influence of NaDC3 deletion outside of the CNS, given that our model also systemically ablates NaDC3. This leaves questions that can only be answered by conditional NaDC3 knockout studies, ongoing in our lab. Our lab is currently exploring CreER^{T2}-mediated conditional knockout of *Slc13a3* to gain insight into the relative contributions of astroglial, meningeal and renal NaDC3 to the preventative effects seen with constitutive deletion.

While renal and astroglial NaDC3 have both been described[27,28,150–152], meningeal NaDC3 remains poorly defined. We were the first to report its expression in Prox1+ meningeal lymphatic cells in mice.[36] Traditionally, meningeal lymphatics were thought to exist primarily in the dura mater[153], but our findings are consistent with recent data from the Nedergaard group regarding a Prox1+ mesothelial membrane existing in the arachnoid space[154] which appears consistent with our published images of a Prox1+/NaDC3+ meningeal layer.[36] The cerebrospinal fluid concentration of NAA is normally around 30 but in Canavan patients it can rise to 300.[15] Given that the NaDC3 K_m for NAA is 250 μM in humans[152], it is possible that strong meningeal contribution to NAA filtration in CSF is limited unless NAA concentrations reach Canavan disease levels. Single cell RNA sequencing data indicates that *Slc13a3* message level is highest in Col1a1+ meningeal fibroblasts[155–157], warranting further study into what role these cells might play in NAA transport.

The established protective benefits of constitutive *Slc13a3* KO—in conjunction with our preliminary results indicating that reversal is possible with conditional *Slc13a3* ablation—support the development of a pharmacological *Slc13a3* inhibitor[158] for testing in human CD patients. Interestingly, administration of lithium, an inhibitor of NaDC3[36,159], reduced whole brain NAA levels by 13% in a CD-like rat model[160] and has been shown to lower NAA levels in Canavan disease

patients.[161,162] It is noteworthy however, that two cases of *Slc13a3* biallelic mutations were associated with brief, reversible episodes of leukoencephalopathy[30], so complete inhibition of the transporter is undesirable. We are encouraged by the strong recovery we saw with even heterozygous *Slc13a3* knockout in CD mice.[36]

5.6 ASTROGLIA IN CANAVAN DISEASE

In Chapter 4, I described marked structural and functional alterations to Bergmann glia in CD mice. Indeed, there are widespread astrocytic changes in CS mice including hypertrophy, astrogliosis[24], and redistribution of aquaporin 4 water channels.[163] Our work showing less frequent and prolonged calcium transients in Bergmann glia processes is the only study to date on astroglial calcium signaling in Canavan disease. Further study in Canavan disease into functional changes in other more ubiquitous astrocyte subtypes would help illuminate further potential glial driven disease mechanisms.

Vacuolar leukodystrophies have traditionally been classified as diseases primarily driven by oligodendroglial mutations and dysfunction however some leukodystrophies like Alexander disease and megalencephalic leukoencephalopathy with subcortical cyst disease are caused by mutations in astroglial specific gene (*Gfap* and *MLC1*, respectively).[164,165]. Astrocyte pathology is observed in many leukodystrophies and indeed, astrocytes have integral roles in oligodendrocyte differentiation, maturation of oligodendrocyte progenitor cells and myelination.

Astrocytes are increasingly becoming recognized as important players in the pathogenesis of a wide range of neurological disorders. As the most ubiquitous glial cell in the brain with expert multitasking abilities, astrocytes represent an important therapeutic target in leukodystrophies and other diseases.

5.7 THE FUTURE OF CANAVAN DISEASE THERAPY

The most direct solution for ASPA deficiency is *Aspa* gene replacement therapy. An early clinical trial conducted in 2000 with an AAV2-Aspa instilled tremendous hope in the Canavan disease community, but ultimately had no lasting effects.[17] The AAV2 was well tolerated but treatment may have been too delayed from the onset of vacuolation or lacking in transduction efficiency or titer.

Two AAV-mediated *Aspa* gene replacement clinical trials are currently recruiting: (1) a Phase 1/2 trial of an AAV9-Aspa treatment developed by *Aspa* Therapeutics, a biotechnology company co-founded by Dr. Guangping Gao a long time Canavan disease researcher[166], and (2) a Phase 1/2 First-In-Human trial utilizing an oligodendrocyte promoter specific rAAV therapy (rAAV_Olig001-Aspa) sponsored by Myrtelle[167], a company named after Dr. Myrtelle Canavan who first described Canavan disease in the 1930s[1]. A recent murine study utilizing a dual approach of AAV-mediated Nat8l knockdown/Aspa gene replacement had promising results, effectively reversing existing pathology in 12 week old CD mice.[168] A Nat8l ASO developed for use in humans might have the potential to become a rapid NAA reduction tool and could be used in conjunction with other gene therapies.

Yanhong Shi's group has recently developed a human induced pluripotent stem cell derived therapy, wherein Canavan disease patient cells are converted back to their pluripotent state, differentiated in neural progenitor cells or oligodendrocyte progenitor cells and then transduced via lentivirus with functional Aspa[56]. These transfected cells are then delivered in CD mice where they engraft and restore normal ASPA activity, lower NAA levels, repair vacuolation and myelination and improve motor function. This approach is also readily translatable to humans.

The most ideal time to intervene in Canavan disease would be prior to symptom onset, which typically occurs at 3-6 months of age. Thus, *in utero* gene editing represents an important early interventional strategy that is currently under investigation through our collaboration with Dr.

Aijun Wang's lab which has expertise in utilizing extracellular vesicles as an intracellular delivery vehicle.

Despite its classification as a rare condition, Canavan disease has a broad and dedicated base of researchers and clinicians invested in developing therapies which hopefully one day make it possible to find a cure for children and families living with this devastating illness.

REFERENCES

1. Canavan, M. M. Schilder's Encephalitis Periaxialis Diffusa: Report of a case in a child aged sixteen and one-half months. *Arch. Neurol. Psychiatry* **25**, 299–308 (1931).
2. van Bogaert & Bertrand I. Sur une idiotie familiale avec degerescence sponglieuse de neuraxe (note preliminaire). *Acta Neurol Belg* 572–87 (1949).
3. Matalon, R. & Michals-Matalon, K. Biochemistry and molecular biology of Canavan disease. *Neurochem. Res.* **24**, 507–513 (1999).
4. Baslow, M. H. Canavan's Spongiform Leukodystrophy : A Clinical Anatomy of a Genetic Metabolic CNS Disease. *J. Mol. Neurosci.* **15**, 61–70 (2000).
5. Merrill, S. T., Nelson, G. R., Longo, N. & Bonkowsky, J. L. Cytotoxic edema and diffusion restriction as an early pathoradiologic marker in canavan disease: case report and review of the literature. *Orphanet J. Rare Dis.* **11**, 169 (2016).
6. Adachi, M., Schneck, L., Cara, J. & Volk, B. W. Spongy degeneration of the central nervous system (van Bogaert and Bertrand type; Canavan's disease). A review. *Hum. Pathol.* **4**, 331–347 (1973).
7. Mirimanoff, P. [Hereditary spongiform dystrophy in young children (Canavan: van Bogaert-Bertrand)]. *J. Neurol. Sci.* **28**, 159–185 (1976).
8. Gambetti, P., Mellman, W. J. & Gonatas, N. K. Familial spongy degeneration of the central nervous system (Van Bogaert-Bertrand disease). An ultrastructural study. *Acta Neuropathol. (Berl.)* **12**, 103–115 (1969).
9. Matalon, R. *et al.* Aspartoacylase deficiency and N-acetylaspartic aciduria in patients with Canavan disease. *Am. J. Med. Genet.* **29**, 463–471 (1988).
10. Kaul, R., Gao, G. P., Balamurugan, K. & Matalon, R. Cloning of the human aspartoacylase cDNA and a common missense mutation in Canavan disease. *Nat. Genet.* **5**, 118–123 (1993).
11. Matalon, R., Michals, K. & Kaul, R. Canavan disease: from spongy degeneration to molecular analysis. *J. Pediatr.* **127**, 511–517 (1995).
12. Janson, C. G. *et al.* Natural history of Canavan disease revealed by proton magnetic resonance spectroscopy (1H-MRS) and diffusion-weighted MRI. *Neuropediatrics* **37**, 209–221 (2006).
13. Bley, A. *et al.* The natural history of Canavan disease: 23 new cases and comparison with patients from literature. *Orphanet J. Rare Dis.* **16**, 227 (2021).
14. Matalon, R. M. & Michals-Matalon, K. Spongy degeneration of the brain, Canavan disease: biochemical and molecular findings. *Front. Biosci. J. Virtual Libr.* **5**, D307-311 (2000).
15. Baslow, M. H. & Guilfoyle, D. N. Canavan disease, a rare early-onset human spongiform leukodystrophy: insights into its genesis and possible clinical interventions. *Biochimie* **95**, 946–956 (2013).
16. Feigenbaum, A. *et al.* Canavan disease: carrier-frequency determination in the Ashkenazi Jewish population and development of a novel molecular diagnostic assay. *Am. J. Med. Genet. A.* **124A**, 142–147 (2004).
17. Leone, P. *et al.* Long-term follow-up after gene therapy for canavan disease. *Sci. Transl. Med.* **4**, 165ra163 (2012).
18. Roscoe, R. B., Elliott, C., Zarros, A. & Baillie, G. S. Non-genetic therapeutic approaches to Canavan disease. *J. Neurol. Sci.* **366**, 116–124 (2016).
19. Francis, J. S. *et al.* N-acetylaspartate supports the energetic demands of developmental myelination via oligodendroglial aspartoacylase. *Neurobiol. Dis.* **96**, 323–334 (2016).

20. Burri, R., Steffen, C. & Herschkowitz, N. N-acetyl-L-aspartate is a major source of acetyl groups for lipid synthesis during rat brain development. *Dev. Neurosci.* **13**, 403–411 (1991).
21. Guo, F. *et al.* Ablating N-acetylaspartate prevents leukodystrophy in a Canavan disease model. *Ann. Neurol.* **77**, 884–888 (2015).
22. Traka, M. *et al.* Nur7 Is a Nonsense Mutation in the Mouse Aspartoacylase Gene That Causes Spongy Degeneration of the CNS. *J. Neurosci.* **28**, 11537–11549 (2008).
23. Martin, E., Capone, A., Schneider, J., Hennig, J. & Thiel, T. Absence of N-acetylaspartate in the human brain: Impact on neurospectroscopy? *Ann. Neurol.* **49**, 518–521 (2001).
24. Bannerman, P. *et al.* Brain Nat8l Knockdown Suppresses Spongiform Leukodystrophy in an Aspartoacylase-Deficient Canavan Disease Mouse Model. *Mol. Ther.* **26**, 793–800 (2018).
25. Hull, V. *et al.* Antisense Oligonucleotide Reverses Leukodystrophy in Canavan Disease Mice. *Ann. Neurol.* **87**, 480–485 (2020).
26. Huang, W. *et al.* Transport of N-Acetylaspartate by the Na$_2$-Dependent High- Affinity Dicarboxylate Transporter NaDC3 and Its Relevance to the Expression of the Transporter in the Brain. **295**, 12 (2000).
27. Fujita, T. *et al.* Transport characteristics of N-acetyl-L-aspartate in rat astrocytes: Involvement of sodium-coupled high-affinity carboxylate transporter NaC3/NaDC3-mediated transport system. *J. Neurochem.* **93**, 706–714 (2005).
28. Sager, T. N., Thomsen, C., Valsborg, J. S., Laursen, H. & Hansen, A. J. Astroglia contain a specific transport mechanism for N-acetyl-L-aspartate. *J. Neurochem.* **73**, 807–811 (1999).
29. Taylor, D. L. *et al.* Extracellular N-Acetylaspartate in the Rat Brain: In Vivo Determination of Basal Levels and Changes Evoked by High K+. *J. Neurochem.* **62**, 2349–2355 (1994).
30. Dewulf, J. P. *et al. SLC13A3* variants cause acute reversible leukoencephalopathy and α-ketoglutarate accumulation: *SLC13A3* Variants. *Ann. Neurol.* **85**, 385–395 (2019).
31. Fasciani, I. *et al.* Directional coupling of oligodendrocyte connexin-47 and astrocyte connexin-43 gap junctions. *Glia* **66**, 2340–2352 (2018).
32. Tress, O. *et al.* Pathologic and Phenotypic Alterations in a Mouse Expressing a Connexin47 Missense Mutation That Causes Pelizaeus-Merzbacher–Like Disease in Humans. *PLoS Genet.* **7**, e1002146 (2011).
33. Lutz, S. E. *et al.* Deletion of Astrocyte Connexins 43 and 30 Leads to a Dysmyelinating Phenotype and Hippocampal CA1 Vacuolation. *J. Neurosci.* **29**, 7743–7752 (2009).
34. Bellamy, T. Interactions between Purkinje neurones and Bergmann glia. *The Cerebellum* **5**, 116–126 (2006).
35. Lordkipanidze, T. & Dunaevsky, A. Purkinje cell dendrites grow in alignment with Bergmann glia. *Glia* **51**, 229–234 (2005).
36. Wang, Y. *et al.* Ablating the Transporter Sodium-Dependent Dicarboxylate Transporter 3 Prevents Leukodystrophy in Canavan Disease Mice. *Ann. Neurol.* **90**, 845–850 (2021).
37. Smith, C. I. E. & Zain, R. Therapeutic Oligonucleotides: State of the Art. *Annu. Rev. Pharmacol. Toxicol.* **59**, 605–630 (2019).
38. Mersmann, N. *et al.* Aspartoacylase-lacZ knockin mice: an engineered model of Canavan disease. *PloS One* **6**, e20336 (2011).
39. Maier, H., Wang-Eckhardt, L., Hartmann, D., Gieselmann, V. & Eckhardt, M. N-Acetylaspartate Synthase Deficiency Corrects the Myelin Phenotype in a Canavan Disease Mouse Model But Does Not Affect Survival Time. *J. Neurosci.* **35**, 14501–14516 (2015).
40. Wiame, E. *et al.* Molecular identification of aspartate N-acetyltransferase and its mutation in hypoacetylaspartia. *Biochem. J.* **425**, 127–136 (2009).

41. Li, S. *et al.* Decreased NAA in Gray Matter is Correlated with Decreased Availability of Acetate in White Matter in Postmortem Multiple Sclerosis Cortex. *Neurochem. Res.* **38**, 2385–2396 (2013).
42. Ahmed, S. S. *et al.* A single intravenous rAAV injection as late as P20 achieves efficacious and sustained CNS Gene therapy in Canavan mice. *Mol. Ther. J. Am. Soc. Gene Ther.* **21**, 2136–2147 (2013).
43. Gessler, D. J. *et al.* Redirecting N-acetylaspartate metabolism in the central nervous system normalizes myelination and rescues Canavan disease. *JCI Insight* **2**, (2017).
44. Sumner, C. J. & Crawford, T. O. Two breakthrough gene-targeted treatments for spinal muscular atrophy: challenges remain. *J. Clin. Invest.* **128**, 3219–3227 (2018).
45. Schoch, K. M. & Miller, T. M. Antisense Oligonucleotides: Translation from Mouse Models to Human Neurodegenerative Diseases. *Neuron* **94**, 1056–1070 (2017).
46. von Jonquieres, G. *et al.* Uncoupling N-acetylaspartate from brain pathology: implications for Canavan disease gene therapy. *Acta Neuropathol. (Berl.)* **135**, 95–113 (2018).
47. Estévez, R. *et al.* Megalencephalic leukoencephalopathy with subcortical cysts: A personal biochemical retrospective. *Eur. J. Med. Genet.* **61**, 50–60 (2018).
48. Sohn, J. *et al.* Suppressing *N* -Acetyl-l-Aspartate Synthesis Prevents Loss of Neurons in a Murine Model of Canavan Leukodystrophy. *J. Neurosci.* **37**, 413–421 (2017).
49. Bergeron. SLC13 family of Na+-coupled di- and tri-carboxylate/sulfate transporters doi:10.1016/j.mam.2012.12.001.
50. Truman, L. A. *et al.* ProxTom Lymphatic Vessel Reporter Mice Reveal Prox1 Expression in the Adrenal Medulla, Megakaryocytes, and Platelets. *Am. J. Pathol.* **180**, 1715–1725 (2012).
51. Bowyer, J. F. *et al.* A visual description of the dissection of the cerebral surface vasculature and associated meninges and the choroid plexus from rat brain. *J. Vis. Exp.* e4285 (2012) doi:10.3791/4285.
52. Zhang, S. *et al.* HIFα Regulates Developmental Myelination Independent of Autocrine Wnt Signaling. *J. Neurosci.* **41**, 251–268 (2021).
53. Moffett, J., Ross, B., Arun, P., Madhavarao, C. & Namboodiri, A. N-Acetylaspartate in the CNS: From neurodiagnostics to neurobiology. *Prog. Neurobiol.* **81**, 89–131 (2007).
54. Louveau, A. *et al.* CNS lymphatic drainage and neuroinflammation are regulated by meningeal lymphatic vasculature. *Nat. Neurosci.* **21**, 1380–1391 (2018).
55. Johnson, N. C. *et al.* Lymphatic endothelial cell identity is reversible and its maintenance requires Prox1 activity. *Genes Dev.* **22**, 3282–3291 (2008).
56. Feng, L. *et al.* Cell-Based Therapy for Canavan Disease Using Human iPSC-Derived NPCs and OPCs. *Adv. Sci. Weinh. Baden-Wurtt. Ger.* **7**, 2002155 (2020).
57. Hoshino, H. & Kubota, M. Canavan disease: Clinical features and recent advances in research. *Pediatr. Int.* **56**, 477–483 (2014).
58. Mendes, M. I. *et al.* Clinically Distinct Phenotypes of Canavan Disease Correlate with Residual Aspartoacylase Enzyme Activity. *Hum. Mutat.* **38**, 524–531 (2017).
59. Ramón y Cajal, S. *Histologie du système nerveux de l'homme & des vertébrés*. 1–1012 (Maloine, 1909). doi:10.5962/bhl.title.48637.
60. Rakic, P. Neuron-glia relationship during granule cell migration in developing cerebellar cortex. A Golgi and electronmicroscopic study in Macacus Rhesus. *J. Comp. Neurol.* **141**, 283–312 (1971).
61. Siegel, A. *et al.* Comparative morphometry of Bergmann glial (Golgi epithelial) cells: A Golgi study. *Anat. Embryol. (Berl.)* **183**, (1991).

62. Grosche, J., Kettenmann, H. & Reichenbach, A. Bergmann glial cells form distinct morphological structures to interact with cerebellar neurons. *J. Neurosci. Res.* **68**, 138–149 (2002).
63. Rakic, P. Mode of cell migration to the superficial layers of fetal monkey neocortex. *J. Comp. Neurol.* **145**, 61–83 (1972).
64. Hartmann, D., Schulze, M. & Sievers, J. Meningeal cells stimulate and direct the migration of cerebellar external granule cells in vitro. *J. Neurocytol.* **27**, 395–409 (1998).
65. Grosche, J. *et al.* Microdomains for neuron–glia interaction: parallel fiber signaling to Bergmann glial cells. *Nat. Neurosci.* **2**, 139–143 (1999).
66. De Zeeuw, C. I. & Hoogland, T. M. Reappraisal of Bergmann glial cells as modulators of cerebellar circuit function. *Front. Cell. Neurosci.* **9**, (2015).
67. Storck, T., Schulte, S., Hofmann, K. & Stoffel, W. Structure, expression, and functional analysis of a Na(+)-dependent glutamate/aspartate transporter from rat brain. *Proc. Natl. Acad. Sci.* **89**, 10955–10959 (1992).
68. Rothstein, J. D. *et al.* Localization of neuronal and glial glutamate transporters. *Neuron* **13**, 713–725 (1994).
69. Bergles, D. E., Dzubay, J. A. & Jahr, C. E. Glutamate transporter currents in Bergmann glial cells follow the time course of extrasynaptic glutamate. *Proc. Natl. Acad. Sci.* **94**, 14821–14825 (1997).
70. Clark, B. A. & Barbour, B. Currents evoked in Bergmann glial cells by parallel fibre stimulation in rat cerebellar slices. *J. Physiol.* **502 (Pt 2)**, 335–350 (1997).
71. Wang, F., Xu, Q., Wang, W., Takano, T. & Nedergaard, M. Bergmann glia modulate cerebellar Purkinje cell bistability via Ca2+-dependent K+ uptake. *Proc. Natl. Acad. Sci.* **109**, 7911–7916 (2012).
72. Burnashev, N. *et al.* Calcium-Permeable AMPA-Kainate Receptors in Fusiform Cerebellar Glial Cells. *Science* **256**, 1566–1570 (1992).
73. Saab, A. S. *et al.* Bergmann Glial AMPA Receptors Are Required for Fine Motor Coordination. *Science* **337**, 749–753 (2012).
74. Müller, T. *et al.* Developmental regulation of voltage-gated K+ channel and GABAA receptor expression in Bergmann glial cells. *J. Neurosci. Off. J. Soc. Neurosci.* **14**, 2503–2514 (1994).
75. Riquelme, R., Miralles, C. P. & De Blas, A. L. Bergmann glia GABA(A) receptors concentrate on the glial processes that wrap inhibitory synapses. *J. Neurosci. Off. J. Soc. Neurosci.* **22**, 10720–10730 (2002).
76. Hoogland, T. M. *et al.* Radially expanding transglial calcium waves in the intact cerebellum. *Proc. Natl. Acad. Sci.* **106**, 3496–3501 (2009).
77. Matsui, K. & Jahr, C. E. Differential control of synaptic and ectopic vesicular release of glutamate. *J. Neurosci. Off. J. Soc. Neurosci.* **24**, 8932–8939 (2004).
78. Beierlein, M. & Regehr, W. G. Brief Bursts of Parallel Fiber Activity Trigger Calcium Signals in Bergmann Glia. *J. Neurosci.* **26**, 6958–6967 (2006).
79. Delaney, C. L., Brenner, M. & Messing, A. Conditional ablation of cerebellar astrocytes in postnatal transgenic mice. *J. Neurosci. Off. J. Soc. Neurosci.* **16**, 6908–6918 (1996).
80. Cui, W., Allen, N. D., Skynner, M., Gusterson, B. & Clark, A. J. Inducible ablation of astrocytes shows that these cells are required for neuronal survival in the adult brain. *Glia* **34**, 272–282 (2001).
81. Cerrato, V. Cerebellar Astrocytes: Much More Than Passive Bystanders In Ataxia Pathophysiology. *J. Clin. Med.* **9**, E757 (2020).
82. Smith, C. I. E. & Zain, R. Therapeutic Oligonucleotides: State of the Art. *Annu. Rev. Pharmacol. Toxicol.* **59**, 605–630 (2019).

83. Guo, F. *et al.* Ablating N-acetylaspartate prevents leukodystrophy in a Canavan disease model. *Ann. Neurol.* **77**, 884–888 (2015).
84. Nimmerjahn, A., Kirchhoff, F., Kerr, J. N. D. & Helmchen, F. Sulforhodamine 101 as a specific marker of astroglia in the neocortex in vivo. 7.
85. Nimmerjahn, A., Mukamel, E. A. & Schnitzer, M. J. Motor Behavior Activates Bergmann Glial Networks. *Neuron* **62**, 400 (2009).
86. Galliano, E. *et al.* Silencing the Majority of Cerebellar Granule Cells Uncovers Their Essential Role in Motor Learning and Consolidation. *Cell Rep.* **3**, 1239–1251 (2013).
87. Hoogland, T. M., De Gruijl, J. R., Witter, L., Canto, C. B. & De Zeeuw, C. I. Role of Synchronous Activation of Cerebellar Purkinje Cell Ensembles in Multi-joint Movement Control. *Curr. Biol.* **25**, 1157–1165 (2015).
88. Vinueza Veloz, M. F. *et al.* Cerebellar control of gait and interlimb coordination. *Brain Struct. Funct.* **220**, 3513–3536 (2015).
89. Ito, M. Historical Review of the Significance of the Cerebellum and the Role of Purkinje Cells in Motor Learning. *Ann. N. Y. Acad. Sci.* **978**, 273–288 (2002).
90. Ito, M. Cerebellar circuitry as a neuronal machine. *Prog. Neurobiol.* **78**, 272–303 (2006).
91. Yamada, K. & Watanabe, M. Cytodifferentiation of bergmann glia and its relationship with purkinje cells. *Anat. Sci. Int.* **77**, 94–108 (2002).
92. Koeppen, A. H. The pathogenesis of spinocerebellar ataxia. *The Cerebellum* **4**, 62–73 (2005).
93. Burright, E. N. *et al.* SCA1 transgenic mice: a model for neurodegeneration caused by an expanded CAG trinucleotide repeat. *Cell* **82**, 937–948 (1995).
94. Custer, S. K. *et al.* Bergmann glia expression of polyglutamine-expanded ataxin-7 produces neurodegeneration by impairing glutamate transport. *Nat. Neurosci.* **9**, 1302–1311 (2006).
95. Shiwaku, H., Yagishita, S., Eishi, Y. & Okazawa, H. Bergmann glia are reduced in spinocerebellar ataxia type 1. *Neuroreport* **24**, 620–625 (2013).
96. Crepel, F., Mariani, J. & Delhaye-Bouchaud, N. Evidence for a multiple innervation of Purkinje cells by climbing fibers in the immature rat cerebellum. *J. Neurobiol.* **7**, 567–578 (1976).
97. Hashimoto, K. & Kano, M. Synapse elimination in the developing cerebellum. *Cell. Mol. Life Sci.* **70**, 4667–4680 (2013).
98. Watanabe, M. & Kano, M. Climbing fiber synapse elimination in cerebellar Purkinje cells. *Eur. J. Neurosci.* **34**, 1697–1710 (2011).
99. Zuo, J. *et al.* Neurodegeneration in Lurcher mice caused by mutation in δ2 glutamate receptor gene. *Nature* **388**, 769–773 (1997).
100. Barnes, J. A. *et al.* Abnormalities in the Climbing Fiber-Purkinje Cell Circuitry Contribute to Neuronal Dysfunction in ATXN1[82Q] Mice. *J. Neurosci.* **31**, 12778–12789 (2011).
101. Ebner, B. A. *et al.* Purkinje Cell Ataxin-1 Modulates Climbing Fiber Synaptic Input in Developing and Adult Mouse Cerebellum. *J. Neurosci.* **33**, 5806–5820 (2013).
102. Hoxha, E., Tempia, F., Lippiello, P. & Miniaci, M. C. Modulation, Plasticity and Pathophysiology of the Parallel Fiber-Purkinje Cell Synapse. *Front. Synaptic Neurosci.* **8**, (2016).
103. Smeets, C. J. L. M., Ma, K. Y., Fisher, S. E. & Verbeek, D. S. Cerebellar developmental deficits underlie neurodegenerative disorder spinocerebellar ataxia type 23. *Brain Pathol. Zurich Switz.* **31**, 239–252 (2021).
104. Lin, C.-Y. *et al.* Abnormal climbing fibre-Purkinje cell synaptic connections in the essential tremor cerebellum. *Brain J. Neurol.* **137**, 3149–3159 (2014).

105. Kuo, S.-H. *et al.* Climbing fiber-Purkinje cell synaptic pathology in tremor and cerebellar degenerative diseases. *Acta Neuropathol. (Berl.)* **133**, 121–138 (2017).
106. Takahashi, M., Sarantis, M. & Attwell, D. Postsynaptic glutamate uptake in rat cerebellar Purkinje cells. *J. Physiol.* **497 (Pt 2)**, 523–530 (1996).
107. Dzubay, J. A. & Jahr, C. E. The Concentration of Synaptically Released Glutamate Outside of the Climbing Fiber–Purkinje Cell Synaptic Cleft. *J. Neurosci.* **19**, 5265–5274 (1999).
108. Brasnjo, G. & Otis, T. S. Neuronal glutamate transporters control activation of postsynaptic metabotropic glutamate receptors and influence cerebellar long-term depression. *Neuron* **31**, 607–616 (2001).
109. Reichelt, W. & Knöpfel, T. Glutamate uptake controls expression of a slow postsynaptic current mediated by mGluRs in cerebellar Purkinje cells. *J. Neurophysiol.* **87**, 1974–1980 (2002).
110. Meldrum, B. & Garthwaite, J. Excitatory amino acid neurotoxicity and neurodegenerative disease. *Trends Pharmacol. Sci.* **11**, 379–387 (1990).
111. Marcaggi, P., Billups, D. & Attwell, D. The role of glial glutamate transporters in maintaining the independent operation of juvenile mouse cerebellar parallel fibre synapses. *J. Physiol.* **552**, 89–107 (2003).
112. Miyazaki, T. *et al.* Glutamate transporter GLAST controls synaptic wrapping by Bergmann glia and ensures proper wiring of Purkinje cells. *Proc. Natl. Acad. Sci. U. S. A.* **114**, 7438–7443 (2017).
113. Rothstein, J. D. *et al.* Knockout of glutamate transporters reveals a major role for astroglial transport in excitotoxicity and clearance of glutamate. *Neuron* **16**, 675–686 (1996).
114. Watase, K. *et al.* Motor discoordination and increased susceptibility to cerebellar injury in GLAST mutant mice. *Eur. J. Neurosci.* **10**, 976–988 (1998).
115. Shibuki, K. *et al.* Deficient cerebellar long-term depression, impaired eyeblink conditioning, and normal motor coordination in GFAP mutant mice. *Neuron* **16**, 587–599 (1996).
116. Lin, X., Antalffy, B., Kang, D., Orr, H. T. & Zoghbi, H. Y. Polyglutamine expansion down-regulates specific neuronal genes before pathologic changes in SCA1. *Nat. Neurosci.* **3**, 157–163 (2000).
117. Perkins, E. M. *et al.* Loss of β-III Spectrin Leads to Purkinje Cell Dysfunction Recapitulating the Behavior and Neuropathology of Spinocerebellar Ataxia Type 5 in Humans. *J. Neurosci.* **30**, 4857–4867 (2010).
118. Sjöbeck, M. & Englund, E. Alzheimer's disease and the cerebellum: a morphologic study on neuronal and glial changes. *Dement. Geriatr. Cogn. Disord.* **12**, 211–218 (2001).
119. Cvetanovic, M. Decreased expression of glutamate transporter GLAST in Bergmann glia is associated with the loss of Purkinje neurons in the spinocerebellar ataxia type 1. *Cerebellum Lond. Engl.* **14**, 8–11 (2015).
120. Auger, C. & Attwell, D. Fast removal of synaptic glutamate by postsynaptic transporters. *Neuron* **28**, 547–558 (2000).
121. Müller, T., Möller, T., Berger, T., Schnitzer, J. & Kettenmann, H. Calcium Entry Through Kainate Receptors and Resulting Potassium-Channel Blockade in Bergmann Glial Cells. *Science* **256**, 1563–1566 (1992).
122. Iino, M. *et al.* Glia-Synapse Interaction Through Ca2+-Permeable AMPA Receptors in Bergmann Glia. *Science* **292**, 926–929 (2001).
123. López-Bayghen, E., Rosas, S., Castelán, F. & Ortega, A. Cerebellar Bergmann glia: an important model to study neuron–glia interactions. *Neuron Glia Biol.* **3**, 155–167 (2007).
124. Ishiuchi, S. *et al.* Extension of glial processes by activation of Ca2+-permeable AMPA receptor channels. *Neuroreport* **12**, 745–748 (2001).

125. Shigetomi, E., Patel, S. & Khakh, B. S. Probing the Complexities of Astrocyte Calcium Signaling. *Trends Cell Biol.* **26**, 300–312 (2016).
126. Sasaki, T. *et al.* Application of an optogenetic byway for perturbing neuronal activity via glial photostimulation. *Proc. Natl. Acad. Sci.* **109**, 20720–20725 (2012).
127. Müller, T., Möller, T., Neuhaus, J. & Kettenmann, H. Electrical coupling among Bergmann glial cells and its modulation by glutamate receptor activation. *Glia* **17**, 274–284 (1996).
128. Nedergaard, M. Direct signaling from astrocytes to neurons in cultures of mammalian brain cells. *Science* **263**, 1768–1771 (1994).
129. Parpura, V. *et al.* Glutamate-mediated astrocyte-neuron signalling. *Nature* **369**, 744–747 (1994).
130. We, K., K, P., J, M., Rj, M. & Jw, P. N-acetyl-L-aspartate and other amino acid metabolites in Alzheimer's disease brain: a preliminary proton nuclear magnetic resonance study. *Neurology* **42**, (1992).
131. Dunlop, D. S., Mc Hale, D. M. & Lajtha, A. Decreased brain N-acetylaspartate in Huntington's disease. *Brain Res.* **580**, 44–48 (1992).
132. Holshouser, B. A. *et al.* Localized proton NMR spectroscopy in the striatum of patients with idiopathic parkinson's disease: a multicenter pilot study. *Magn. Reson. Med.* **33**, 589–594 (1995).
133. Blasco, H. *et al.* Understanding and managing metabolic dysfunction in Amyotrophic Lateral Sclerosis. *Expert Rev. Neurother.* **20**, 907–919 (2020).
134. Jasperse, B. *et al.* N-acetylaspartic acid in cerebrospinal fluid of multiple sclerosis patients determined by gas-chromatography-mass spectrometry. *J. Neurol.* **254**, 631–637 (2007).
135. Moffett, J. R., Arun, P., Ariyannur, P. S. & Namboodiri, A. M. A. N-Acetylaspartate reductions in brain injury: impact on post-injury neuroenergetics, lipid synthesis, and protein acetylation. *Front. Neuroenergetics* **5**, 11 (2013).
136. Lai, M. L., Hsu, Y. I., Ma, S. & Yu, C. Y. Magnetic resonance spectroscopic findings in patients with subcortical ischemic stroke. *Zhonghua Yi Xue Za Zhi Chin. Med. J. Free China Ed* **56**, 31–35 (1995).
137. Magnetic Resonance Spectroscopy in Epilepsy: Clinical Issues - Cendes - 2002 - Epilepsia - Wiley Online Library. https://onlinelibrary.wiley.com/doi/full/10.1046/j.1528-1157.2002.043s1032.x.
138. Lanznaster, D., Dingeo, G., Samey, R. A., Emond, P. & Blasco, H. Metabolomics as a Crucial Tool to Develop New Therapeutic Strategies for Neurodegenerative Diseases. *Metabolites* **12**, 864 (2022).
139. Appu, A. P. *et al.* Increasing N-acetylaspartate in the Brain during Postnatal Myelination Does Not Cause the CNS Pathologies of Canavan Disease. *Front. Mol. Neurosci.* **10**, (2017).
140. Tranberg, M. & Sandberg, M. N-Acetylaspartate monomethyl ester increases N-acetylaspartate concentration in cultured rat hippocampal slices: Effects on excitotoxicity and levels of amino acids and chloride. *J. Neurosci. Methods* **163**, 105–110 (2007).
141. Kolodziejczyk, K., Hamilton, N. B., Wade, A., Káradóttir, R. & Attwell, D. The effect of N-acetyl-aspartyl-glutamate and N-acetyl-aspartate on white matter oligodendrocytes. *Brain J. Neurol.* **132**, 1496–1508 (2009).
142. Neale, J. H., Bzdega, T. & Wroblewska, B. N-acetylaspartylglutamate: The most abundant peptide neurotransmitter in the mammalian central nervous system. *J. Neurochem.* **75**, 443–452 (2000).
143. Khacho, P., Wang, B., Ahlskog, N., Hristova, E. & Bergeron, R. Differential effects of N-acetyl-aspartyl-glutamate on synaptic and extrasynaptic NMDA receptors are subunit- and

pH-dependent in the CA1 region of the mouse hippocampus. *Neurobiol. Dis.* **82**, 580–592 (2015).
144. Morland, C. & Nordengen, K. N-Acetyl-Aspartyl-Glutamate in Brain Health and Disease. *Int. J. Mol. Sci.* **23**, 1268 (2022).
145. *N-Acetylaspartate: A Unique Neuronal Molecule in the Central Nervous System*. vol. 576 (Springer US, 2006).
146. Carpenter, K. J. *et al.* Effects of GCP-II inhibition on responses of dorsal horn neurones after inflammation and neuropathy: an electrophysiological study in the rat. *Neuropeptides* **37**, 298–306 (2003).
147. Yamamoto, T., Kozikowski, A., Zhou, J. & Neale, J. H. Intracerebroventricular administration of N-acetylaspartylglutamate (NAAG) peptidase inhibitors is analgesic in inflammatory pain. *Mol. Pain* **4**, 31 (2008).
148. Zhou J, Neale JH, Pomper MG, Kozikowski AP. NAAG peptidase inhibitors and their potential for diagnosis and therapy. *Nat Rev Drug Discov* (2005).
149. Nguyen, T. *et al.* Uncovering the Role of N-Acetyl-Aspartyl-Glutamate as a Glutamate Reservoir in Cancer. *Cell Rep.* **27**, 491-501.e6 (2019).
150. Breljak, D. *et al.* Distribution of organic anion transporters NaDC3 and OAT1-3 along the human nephron. *Am. J. Physiol.-Ren. Physiol.* **311**, F227–F238 (2016).
151. Burckhardt, B. C. *et al.* The renal Na(+)-dependent dicarboxylate transporter, NaDC-3, translocates dimethyl- and disulfhydryl-compounds and contributes to renal heavy metal detoxification. *J. Am. Soc. Nephrol. JASN* **13**, 2628–2638 (2002).
152. George, R. L., Huang, W., Naggar, H. A., Smith, S. B. & Ganapathy, V. Transport of N-acetylaspartate via murine sodium/dicarboxylate cotransporter NaDC3 and expression of this transporter and aspartoacylase II in ocular tissues in mouse. *Biochim. Biophys. Acta BBA - Mol. Basis Dis.* **1690**, 63–69 (2004).
153. Louveau, A. *et al.* Structural and functional features of central nervous system lymphatics. *Nature* **523**, 337–341 (2015).
154. Møllgård, K. *et al.* A mesothelium divides the subarachnoid space into functional compartments. *Science* **379**, 84–88 (2023).
155. DeSisto, J. *et al.* Single-Cell Transcriptomic Analyses of the Developing Meninges Reveal Meningeal Fibroblast Diversity and Function. *Dev. Cell* **54**, 43-59.e4 (2020).
156. Kozareva, V. *et al.* A transcriptomic atlas of mouse cerebellar cortex comprehensively defines cell types. *Nature* **598**, 214–219 (2021).
157. Yao, Z. *et al.* A taxonomy of transcriptomic cell types across the isocortex and hippocampal formation. *Cell* **184**, 3222-3241.e26 (2021).
158. Wei, H. *et al.* The pathogenesis of, and pharmacological treatment for, Canavan disease. *Drug Discov. Today* **27**, 2467–2483 (2022).
159. Chen, X., Tsukaguchi, H., Chen, X.-Z., Berger, U. V. & Hediger, M. A. Molecular and functional analysis of SDCT2, a novel rat sodium-dependent dicarboxylate transporter. *J. Clin. Invest.* **103**, 1159–1168 (1999).
160. The Effects of Lithium Chloride and Other Substances on Levels of Brain N-Acetyl-L-Aspartic Acid in Canavan Disease-Like Rats | SpringerLink. https://link.springer.com/article/10.1023/A:1015504031229.
161. Janson, C. G. *et al.* Lithium citrate for Canavan disease. *Pediatr. Neurol.* **33**, 235–243 (2005).
162. Assadi, M. *et al.* Lithium citrate reduces excessive intra-cerebral N-acetyl aspartate in Canavan disease. *Eur. J. Paediatr. Neurol. EJPN Off. J. Eur. Paediatr. Neurol. Soc.* **14**, 354–359 (2010).

163. Clarner, T. *et al.* Astroglial redistribution of aquaporin 4 during spongy degeneration in a Canavan disease mouse model. *J. Mol. Neurosci. MN* **53**, 22–30 (2014).
164. Lanciotti, A., Brignone, M. S., Macioce, P., Visentin, S. & Ambrosini, E. Human iPSC-Derived Astrocytes: A Powerful Tool to Study Primary Astrocyte Dysfunction in the Pathogenesis of Rare Leukodystrophies. *Int. J. Mol. Sci.* **23**, 274 (2022).
165. Mlc1-Expressing Perivascular Astrocytes Promote Blood-Brain Barrier Integrity - PubMed. https://pubmed.ncbi.nlm.nih.gov/34965971/.
166. Aspa Therapeutics. *A Phase 1/2 Open-Label Study of the Safety and Clinical Activity of Gene Therapy for Canavan Disease Through Administration of an Adeno-Associated Virus (AAV) Serotype 9-Based Recombinant Vector Encoding the Human ASPA Gene*. https://clinicaltrials.gov/ct2/show/NCT04998396 (2023).
167. Myrtelle Inc. *Phase 1/2, Open Label, Sequential Cohort Study of a Single Intracranial Dose of AVASPA Gene Therapy for Treatment of Children With Typical Canavan Disease*. https://clinicaltrials.gov/ct2/show/NCT04833907 (2023).
168. Fröhlich, D. *et al.* Dual-function AAV gene therapy reverses late-stage Canavan disease pathology in mice. *Front. Mol. Neurosci.* **15**, 1061257 (2022).